Title

The Relationship Between Convective Clustering and Mean Tropical Climate in Aquaplanet Simulations

Journal

Journal of Advances in Modeling Earth Systems, 12(8)

ISSN

1942-2466

Authors

Popp, Max
Lutsko, Nicholas J
Bony, Sandrine

Publication Date

2020-08-01

DOI

10.1029/2020ms002070

Peer reviewed

AGU ADVANCING EARTH AND SPACE SCIENCE

JAMES Journal of Advances in Modeling Earth Systems

RESEARCH ARTICLE
10.1029/2020MS002070

Key Points:
- The impact of convective clustering on tropical climate depends on both the total convecting area and on the number of convective clusters
- The total convective area affects the meridional distribution of water; the number of convective regions affects the zonal variance of water
- Many findings from radiative convective equilibrium studies are confirmed in aquaplanet simulations with realistic sea surface temperatures

Correspondence to:
M. Popp,
max.popp@lmd.jussieu.fr

Citation:
Popp, M., Lutsko, N. J., & Bony, S. (2020). The relationship between convective clustering and mean tropical climate in aquaplanet simulations. *Journal of Advances in Modeling Earth Systems*, *12*, e2020MS002070. https://doi.org/10.1029/2020MS002070

Received 4 FEB 2020
Accepted 4 JUL 2020
Accepted article online 9 JUL 2020

The Relationship Between Convective Clustering and Mean Tropical Climate in Aquaplanet Simulations

Max Popp[1], **Nicholas J. Lutsko**[2], **and Sandrine Bony**[1]

[1]Laboratoire de Météorologie Dynamique (LMD/IPSL), Sorbonne Université, Centre National de la Recherche Scientifique (CNRS), École Polytechnique, École Normale Supérieure, Paris, France, [2]Scripps Institution of Oceanography, University of California, San Diego, La Jolla, CA, USA

Abstract Convective clustering, the spatial organization of tropical deep convection, can manifest itself in two ways: through a decrease in the total area covered by convection and/or through a decrease in the number of convective areas. Much of our current understanding of convective clustering comes from simulations in idealized radiative convective equilibrium (RCE) configurations. In these simulations the two forms of convective clustering tend to covary, and their individual effects on the climate are thus hard to disentangle. This study shows that in aquaplanet simulations with more realistic boundary conditions, such as meridional gradients of surface temperature and rotational forces, the two aspects of convective clustering are not equivalent and are associated with different impacts on the large-scale climate. For instance, reducing the convective area in the equatorial region in the aquaplanet simulations results in broader meridional humidity and rain distributions and in lower tropospheric temperatures throughout the tropics. By contrast, the number of convective regions primarily impacts the zonal variance of humidity-related quantities in the aquaplanet simulations, as the distribution of convective regions affects the size of the subsidence regions and thereby the moistening influence of convective regions. The aquaplanet simulations confirm many other qualitative results from RCE simulations, such as a reduction of equatorial tropospheric humidity when the area covered by convection diminishes.

Plain Language Summary Strong precipitation events in Earth's tropics are associated with regions of strong upward motions that can extend over the entire depth of the troposphere. These regions of strong upward motions are not uniformly distributed throughout the tropics but occur mostly as clusters of various shapes and sizes, typically within a narrow zonal band. We show here with idealized climate simulations that different forms of spatial organization of the regions of upward motions have distinct impacts on the climate, highlighting the need to consider several metrics to characterize the organization. For instance, reducing the area covered by upward motions close to the equator results in broader meridional humidity and rain distributions. By contrast, the number of regions of upward motion primarily impacts the zonal variance of humidity-related quantities.

1. Introduction

A striking feature of Earth's tropics when observed from space is the various spatial patterns of deep convection that appear as areas of high cloud cover within the tropical rain belt. These patterns consist of deep convective clusters of various sizes and shapes (Mapes & Houze, 1993; Tobin et al., 2012) that are separated by regions of clear sky or low cloud cover associated with subsiding motions. The sizes of the clusters range from a few kilometers (e.g., Houze, 1977; Laing & Fritsch, 1997) to large-scale patterns such as can be seen during the Madden Julian Oscillation (MJO; Arnold & Randall, 2015; Madden & Julian, 1971, 1994). Recent observational results suggest that the form of this convective clustering has a large impact on the tropical climate (Holloway et al., 2017; Popp & Bony, 2019; Semie & Bony, 2020; Tobin et al., 2012).

Most of our current understanding of self-organization of convection comes from idealized climate simulations with horizontally uniform boundary conditions (and without planetary rotation), the so-called radiative convective equilibrium (RCE). If certain conditions are met in this type of experiment, the convection spontaneously self organizes, leading to a decrease in the number of convective regions and in the total area covered by convection (Bretherton et al., 2005; Coppin & Bony, 2017, 2015; Held et al., 1993; C. J. Muller & Held, 2012; C. Muller & Bony, 2015; Tompkins & Craig, 1998; Wing & Emanuel, 2014; Wing et al., 2017).

The conditions and mechanisms of self-organization and of the convective clustering have been extensively studied in RCE configurations, but there are many open questions as to how the results of RCE simulations translate to more realistic configurations and whether the same mechanisms are at work.

To better understand the link between RCE and more realistic configurations with planetary rotation and meridional temperature gradients, we analyze aquaplanet simulations first described in Popp and Bony (2019) (henceforth PB19). In these simulations, different forms of zonal convective clustering were prescribed in an equatorial band, with the aim of understanding the impact of zonal convective clustering on the width of the tropical rain belt. However, the results of these experiments can be used to investigate a number of other important questions, such as the impact of the zonal convective clustering on the mean thermodynamic state of the tropical atmosphere and the separate impacts of the number convective regions and of the total area covered by convective regions. These topics are covered in the present manuscript. We choose to focus on the effects of the convective clustering on the temporal mean climate response, as this aspect of the response is readily comparable to previous RCE domain mean results. This analysis will thus allow us to compare the impacts of the convective clustering on the temporal mean climate in the aquaplanet simulations with those found in RCE simulations. Together, these analyses expand on previous RCE results by providing insights into the links between the two different forms of convective clustering and the large-scale climate of the tropics in a more realistic configuration.

The paper is organized as follows: we summarize the experimental design of the analyzed experiments in the following section and define two metrics for convective clustering, related to the area of convection and to the number of convective regions, respectively, in section 3. In section 4 we use the two metrics to characterize the impacts of convective clustering on the tropical climate and then examine the mechanisms by which clustering influences the climate in section 5. In section 6we compare the employed metrics for convective clustering to other metrics, compare the aquaplanet simulations with previous RCE results, address limitations of the employed model setup, and discuss potential follow-up analyses. Finally, we summarize our main findings in section 7.

2. Experimental Design

We outline the experimental design below and refer the reader to the methods section of PB19 for more details.

2.1. Climate Model and Boundary Conditions

Simulations were performed with Version 5A of the atmospheric component of the Institute Pierre Simon Laplace (IPSL) coupled model IPSL-CM5A-MR (Dufresne, 2013; Hourdin et al., 2006; Hourdin, 2013). This medium-resolution version of the model (MR, 1.25° × 2.53° horizontal resolution) also took part in the Climate Model Intercomparison Project Phase 5 (CMIP5 Taylor et al., 2012). The model uses hybrid sigma pressure coordinates in the vertical and resolves the atmosphere with 39 levels up to a height of approximately 70 km. Simulations were performed on a rotating aquaplanet, meaning that all continents were removed and replaced by sea surface conditions. Perpetual equinox conditions, which assume a daily cycle but no seasonal cycle, and a top-of-atmosphere insolation that is equivalent to 1,366 $\mathrm{W\,m^{-2}}$ were imposed. Sea surface temperatures were prescribed to be zonally uniform and to include meridional gradients to mimic Earth's mean meridional temperature gradients, following the aquaplanet experiment (APE) protocol, except for the use of the “control” sea surface temperature distribution instead of “QOBS” (Neale & Hoskins, 2000; Williamson, 2012).

2.2. Evaporation Patterns

Convection tends to localize over maxima of boundary layer moist static energy (MSE; Emanuel et al., 1994; Lindzen & Hou, 1988; Möbis & Stevens, 2012; Privé & Plumb, 2007; Popp & Silvers 2017), which implies that the spatial organization of convection can be prescribed by imposing evaporation patterns: Regions of enhanced (reduced) evaporation receive an additional (reduced) influx of MSE and hence have maxima (minimum) in the boundary layer MSE. With this methodology we can thus control the size and the number of convective clusters. Using the evaporation to force changes in convective clustering also has the advantage of constraining the global mean precipitation, as the global mean precipitation must be balanced by the global mean evaporation in a steady state.

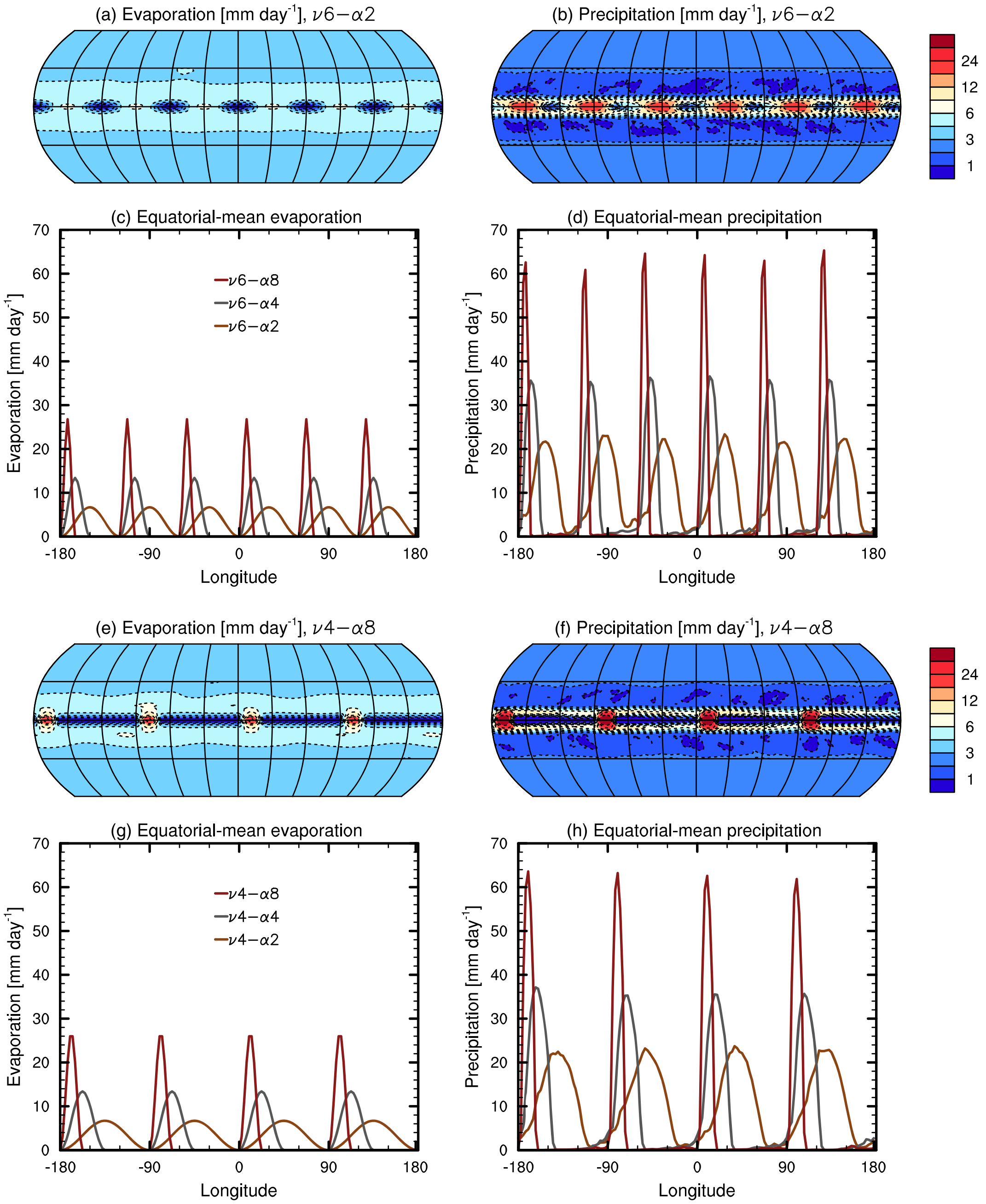

Figure 1. Panel (a) shows the temporal mean evaporation in the ν6-α2 experiment (with forced evaporation from 10°S to 10°N). Panel (b) shows the same but for the precipitation instead of the evaporation. Panel (c) shows the temporal mean evaporation as a function of longitude at the equator for the three employed amplitudes corresponding to 2, 4, and 8 times the zonal-mean value (all for ν6). Note that since the zonal mean of the imposed evaporation patterns is the same in all simulations, a larger amplitude implies a spatial contraction of the regions of increased evaporation. Panel (d) shows the same as (c) but for the temporal mean precipitation. Panel (e) shows the same as (a), and Panel (f) as (b) but for the ν4-α8 experiment. Panel (g) shows the same as (c), and Panel (h) as (d) for the ν4 experiments.

In the analyzed experiments the evaporation is relaxed toward an imposed pattern using Newtonian relaxation, with the relaxation time scale being instantaneous at the equator and then decreasing with latitude within a band from 10°S to 10°N; at higher latitudes the evaporation evolves freely. The imposed evaporation pattern is zonally periodic and is controlled by two parameters: the amplitude of the periodic variations α, and the zonal wavenumber ν. The zonal means of the imposed evaporation fields are kept fixed in all

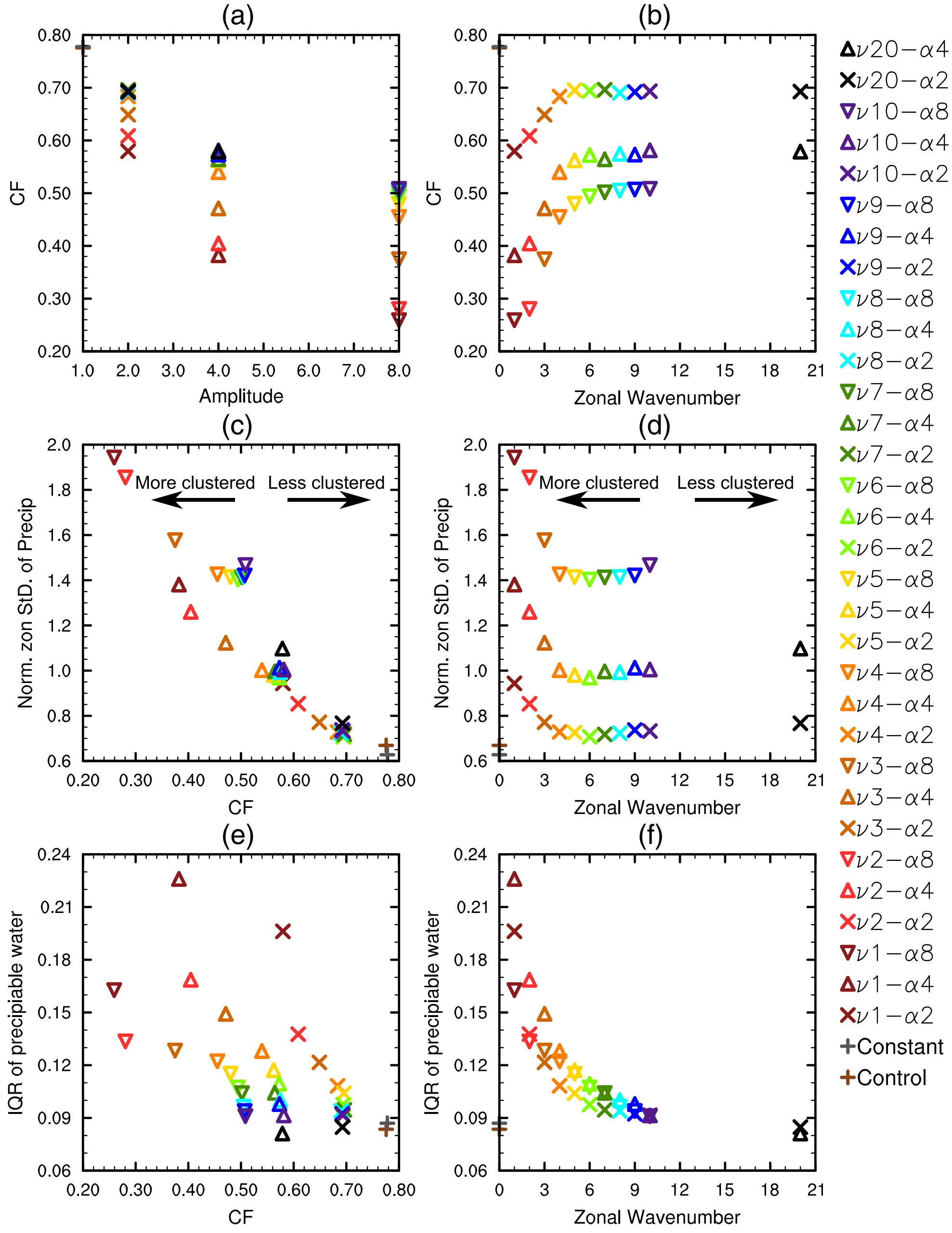

Figure 2. Panel (a) shows the steady-state CF as a function of the amplitude of the imposed forcing. Panel (c) shows the normalized zonal standard deviation of precipitation from 6°S to 6°N ($\overline{S_\lambda(P)}$) and Panel (e) the interquartile ratio (IQR) of precipitable water as a function of CF in the mean over the steady-state period. Panel (b) shows the steady-state CF, Panel (d) the steady-state normalized zonal standard deviation of precipitation from 6°S to 6°N ($\overline{S_\lambda(P)}$), and Panel (f) the steady-state IQR of precipitable water all as a function of the zonal wavenumber where the CONTROL and CONSTANT experiments are plotted as Wavenumber 0.

experiments, so that the zonal mean evaporation in the deep tropics is approximately constant across the experiments, and a lower bound of 0 for the evaporation is also imposed. These two requirements mean that the total convective area must shrink as α is increased: increasing the evaporation at some longitudes means that the total evaporation area along a longitude circle must decrease. Increasing ν increases the number of convecting regions. Note that the amplitude of the imposed evaporation pattern also decreases with latitude, producing a smooth transition from the regions with forced evaporation to the regions with freely evolving evaporation.

Two examples of the imposed evaporation fields and the precipitation responses are given in Figure 1, and a full mathematical description of the evaporation fields is given in PB19.

2.3. Experiments

Experiments were performed for a range of α and ν, with each experiment lasting for 1,080 (3×360) days and the first 360 days discarded. A control experiment (henceforth CONTROL) was run in which the evaporation was unforced; that is, the evaporation is calculated interactively. The state of CONTROL after 360 days was then used as the initial condition for the other experiments. These are composed of one experiment with a zonally uniform forced evaporation field (CONSTANT) and 30 experiments with forced evaporation fields that are periodic in the zonal direction with zonal wavenumbers (ν) from 1 to 10 and amplitudes (α) 2, 4, and 8 for each value of ν. The values of α correspond to the maximum of the imposed evaporation pattern along the equator and are expressed as multiples of the equatorial mean evaporation. So $\alpha = 4$ means that the maximum evaporation along the equator is 4 times the equatorial mean evaporation. Two sensitivity experiments with $\nu = 20$ and $\alpha = 2{,}4$ were also performed for sensitivity purposes, to make 34 experiments in total. Note that an experiment with $\nu = 20$ and $\alpha = 8$ would have confined the individual convective regions to less than a grid point and was thus not performed.

We will henceforth denote the experiments based on their values of ν and α. So experiment $\nu3$-$\alpha4$ refers to the experiment with $\nu = 3$ and $\alpha = 4$. To refer to all experiments with a given amplitude, we will refer to the $\alpha2$ experiments, the $\alpha4$ experiments, etc. Likewise we will refer to the $\nu1,\nu2,\ldots,\nu10$ experiments for all experiments with a given wavenumber.

In this framework, the experiments were designed such that smaller values of the wavenumber ν and higher values of the amplitude α of the evaporation (and thus of the convective) pattern each correspond to more zonally “clustered” states (we define “clustering” more precisely below).

3. Metrics for Convective Clustering and Other Conventions

Our experimental setup allows us to separately vary the zonal wavenumber and the amplitude of the evaporation forcing, giving us two degrees of freedom by which the zonal distribution of convection can be varied. Our goal is for the zonal wavenumber to control the number of individual convecting regions and for the amplitude to control the total area covered by convection. With this idea in mind, we have defined two principal metrics to quantify the separate influences of the number of convective regions and of the total area covered by convection on the tropical climate.

Since in our experimental setup the convective regions are forced to be evenly distributed along the equator, the spatial distribution of the convective regions can be effectively characterized by the number of convective regions, with a higher number of convective regions implying that the regions are more evenly distributed along the equator. Because of the high spatial correlation between the imposed evaporation and precipitation in the deep tropics of the analyzed simulations (PB19, see also Figure 1), the number of convective regions corresponds to the zonal wavenumber of the forcing. Therefore, we use the zonal wavenumber as the metric to characterize the zonal distribution along the equator. With this metric a “more clustered” state corresponds to a lower wavenumber and hence a state with fewer convective regions. We will henceforth use zonal wavenumber and number of convective regions interchangeably.

To quantify the total area covered by convection—its spatial concentration—we define the convective fraction (CF) as the zonal fraction of negative values of the meridional mean vertical pressure velocity at 500 hPa (i.e., $\omega(p = 500\,\text{hpa}) < 0$) between 6°S and 6°N. The CF is strongly controlled by the amplitude of the imposed forcing (Figure 2a), confirming that changing the amplitude is indeed a powerful way to change the overall CF and thus the spatial concentration of convection. With this metric a “more clustered” state corresponds to a lower CF.

The CF also increases with the zonal wavenumber for $\nu < 4$–5 (Figure 2b) and then appears to saturate at higher wavenumber (the value at which it saturates is dependent on the value of α). So the two metrics are not strictly independent in our experimental setup, and we will take this into account in our analysis. We therefore expect that quantities that depend on CF also depend on the zonal wavenumber for $\nu < 4$–5. This dependence is an undesired effect of the experimental setup. In order to obtain the explicit dependence of quantities on the wavenumber, independent of the CF, we have two possibilities. One possibility is to

Table 1

Variance Explained Between the Convective Fraction (CF), the Zonal Wavenumber (ν), the Average Subsidence Length (L_D), and Other Climate Indicators in the 34 Simulations Averaged Over the Steady-State Period and Over the Zonal Band From 6°S to 6°N

	CF	ν	L_D
$\overline{S_\lambda(P)}$	(−) 89%	(−) 8%	(+) 30%
IQR	(−) 34%	(−) 51%	(+) 76%
Zonal wavenumber	(+) 6%	(+) 100%	(−) 34%
Precipitable water	(+) 92%	(+) 36%	(−) 69%
Condensed water path	(+) 93%	(+) 7%	(−) 33%
Total cloud fraction	(+) 82%	(+) 41%	(−) 70%
High cloud fraction	(+) 84%	(+) 42%	(−) 64%
Atmospheric energy uptake	(+) 73%	(+) 49%	(−) 49%
Cloud-radiative effect	(+) 87%	(+) 40%	(−) 65%
Clear-sky atmospheric energy uptake	(−) 85%	(−) 4%	(+) 65%
Albedo	(+) 90%	(+) 25%	(−) 63%
500 hPa temperature	(+) 78%	(+) 8%	(−) 6%
200 hPa zonal wind	(−) 42%	(−) 35%	(+) 99%

Note. $\overline{S_\lambda(P)}$ denotes the temporal mean of the meridionally averaged zonal standard deviation of precipitation from 6°S to 6°N divided by the mean precipitation over the same area and IQR the interquartile ratio of precipitable water. The average zonal subsidence size (L_D) was estimated by taking $360°\cdot(1-\mathrm{CF})/\nu$. Note that for the correlations between the zonal wavenumber (ν) and other quantities as well as for the correlations between the average zonal subsidence size (L_D) and other quantities, the CONTROL and the CONSTANT experiments were excluded, as it is not clear to what values they correspond.

focus on the zonal wavenumbers for $\nu>5$, where the wavenumber and the CF are independent of each other and where thus only the explicit dependence of quantities on the wavenumber appears. The other possibility is to remove the implicit influence of the wavenumber through its influence on CF, and we developed a methodology for this purpose that is described in Appendix A. We will apply this methodology and show the modified results below.

Henceforth, we will refer to the region from 30°S to 30°N as the "tropical region" and accordingly tropical as an adjective will refer to this region. We will refer to region from 6°S to 6°N as the "equatorial region," and accordingly the adjective equatorial will refer to this region.

4. Relationships Between Different Forms of Convective Clustering and the Temporal Mean Tropical Climate

We start our results section by showing the primary impacts of changing zonal convective clustering by changing CF and by changing the number of convective regions individually. We then discuss a more focused analysis of the impacts of convective clustering (defined in either way) on the meridional aspects of the response.

4.1. Increased Convective Clustering Associated With a Reduced Convective Fraction

In this first paragraph we review the results of PB19 on how the convective fraction affects different aspects of the tropical climate, before showing new additional results in the second paragraph of this subsection. PB19 showed most of the results as a function of a precipitation-based metric ($\overline{S_\lambda(P)}$), but this precipitation-based metric is highly correlated with the CF (Table 1), and thus the relations they found with $\overline{S_\lambda(P)}$ carry directly over to CF. Their main result is a widening of the ITCZ with increased convective clustering by decreasing the CF (their Figure 2, and Figure 3b of this manuscript). They also showed that increasing the convective clustering in this manner decreases the precipitation and the cloud fraction in the equatorial region, which leads to a decrease in cloud-radiative heating that contributes to a reduction of the atmospheric energy uptake in the equatorial region (see their Figures 2 and 6, and also Figure 3a and Table 1 of this manuscript). They then suggested that this leads to a reduction of the meridional energy transport, to a weakening of the meridional overturning circulation, and to a widening of the ITCZ. They also showed that stronger convective clustering was associated with weaker meridional but stronger zonal moisture convergence in the equatorial region (their Figure 4).

Additional, new analysis demonstrates here that increasing the convective clustering by reducing the CF also leads to a cooling of the free troposphere (Figure 3g), to a decrease in precipitable and condensed water paths (Figures 3c and 3e), and to a reduction in albedo in the equatorial region (Table 1). This decrease in precipitable water is not only due to the larger area fraction covered by subsidence with stronger convective clustering, but also to a decrease of precipitable water within the convective (and within the subsidence) regions with stronger convective clustering (not shown). The changes in the tropical mean (defined here as the average from 30°S to 30°N) of the water-related quantities are substantially smaller than the changes in the equatorial mean (compare Figures 3d and 3c as well as Figures 3f and 3e), because the effects on the equatorial region are countered at higher tropical latitudes (mostly between 6° and 20° latitude, Figures 4a–4d). The tropospheric temperature, by contrast, also decreases in the tropical mean with decreasing CF (Figure 3h). This can be expected because gravity waves tend to even out horizontal inhomogeneities where the Coriolis parameter is small (Sobel & Bretherton, 2000), which is the case for most of the tropics (Figure 4e).

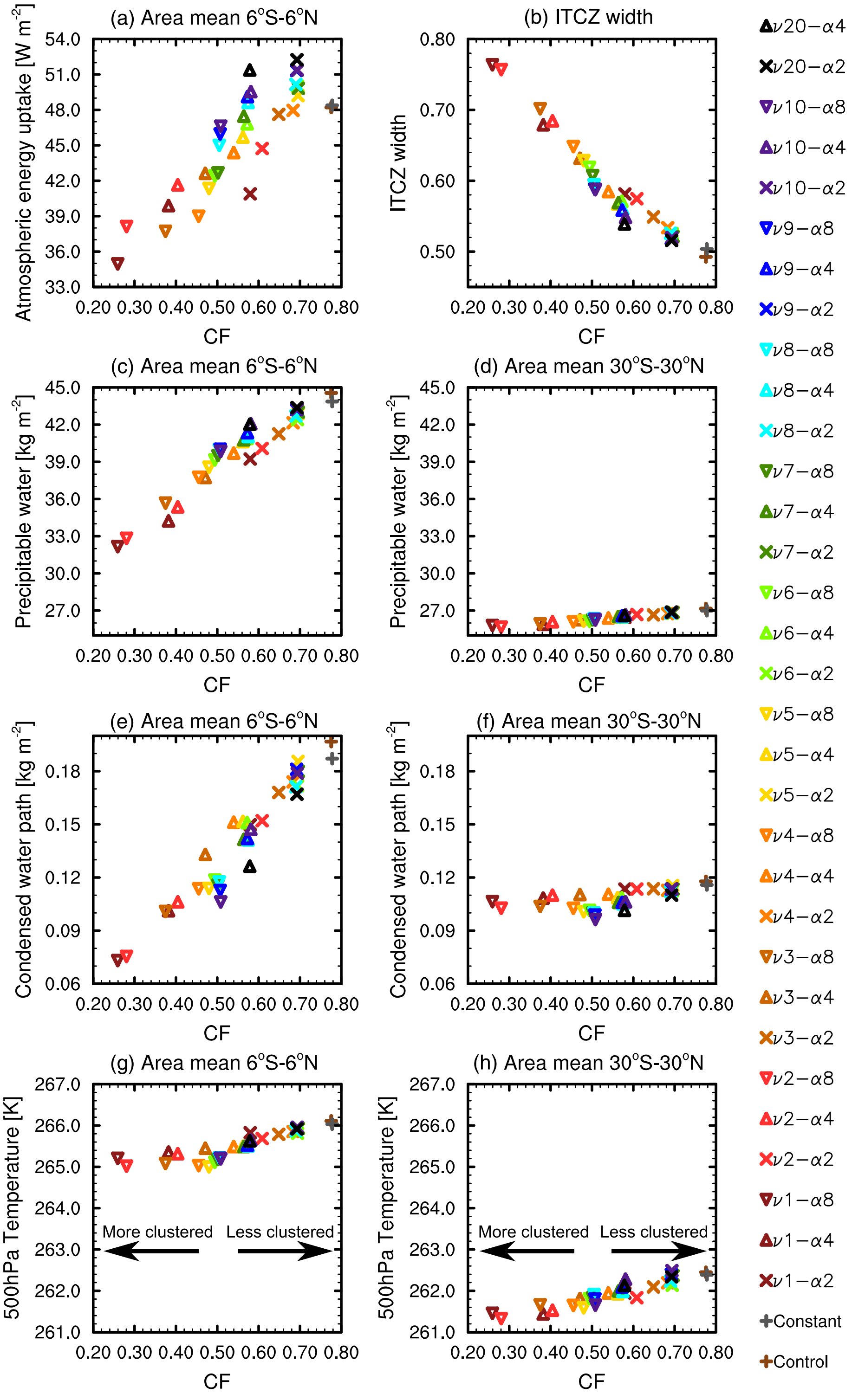

Figure 3. Panel (a) shows the steady-state mean atmospheric energy uptake in the zonal band from 6°S to 6°N as a function of the convective fraction CF. Panel (b) shows the ITCZ width, inferred by taking the mean precipitation of the zonal band from 15°S to 15°N and dividing it by the mean precipitation in the zonal band from 6°S to 6°N. Panels (c) and (d) show the vertically integrated steady-state precipitable water, Panels (e) and (f) the vertically integrated steady-state condensed water path, and Panels (g) and (h) the steady-state temperature at the 500 hPa pressure level, all as a function of the convective fraction (CF). The left column (Panels c, e, and g) shows the area mean of the variables on the ordinate in the zonal band from 6°S to 6°N. The right column (Panels d, f, and h) shows the area mean of the variables on the ordinate in the zonal band from 30°S to 30°N.

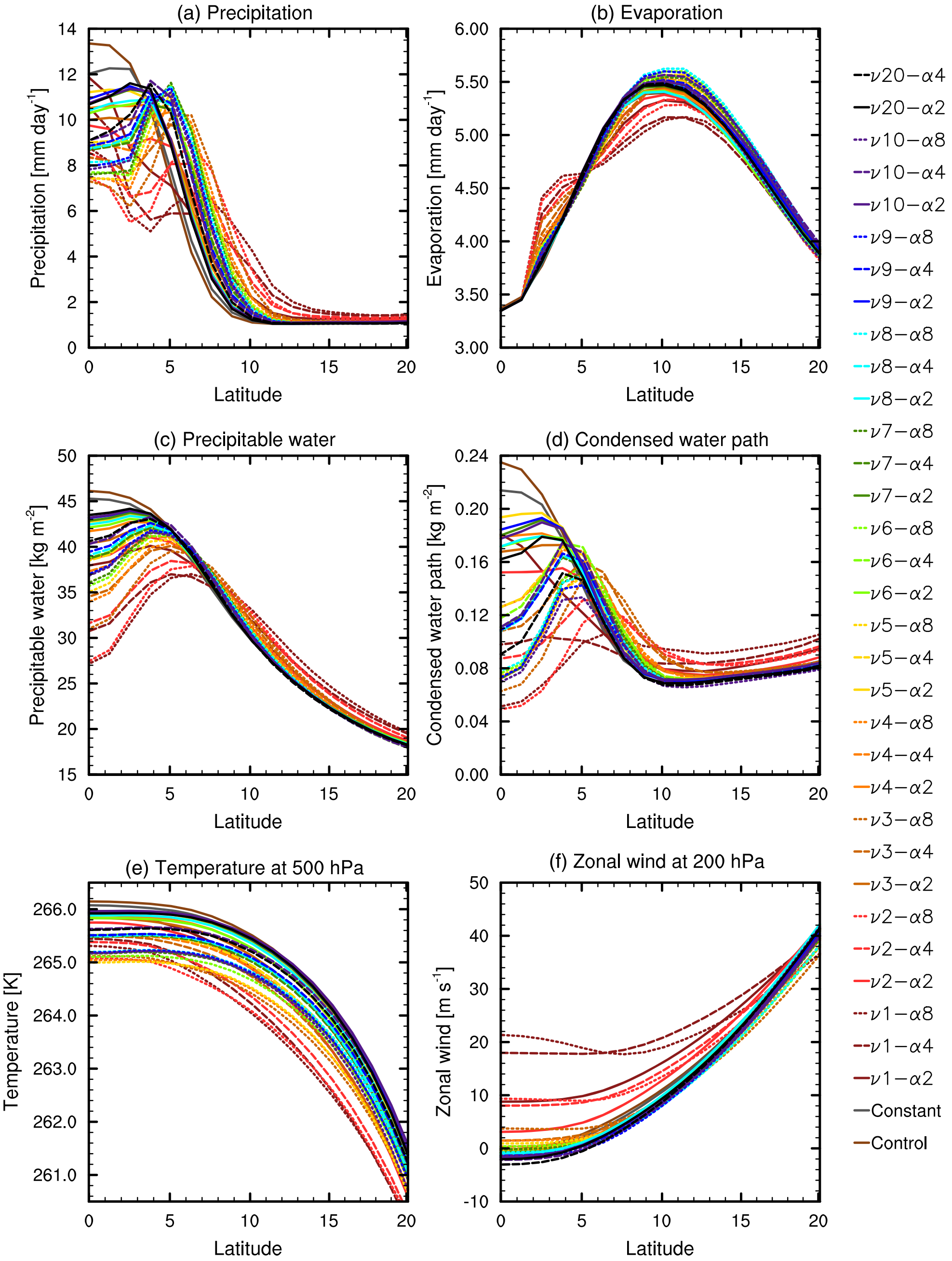

Figure 4. Panel (a) shows the steady-state and zonal means of the precipitation, Panel (b) of the evaporation, Panel (c) of the precipitable water, Panel (d) of the condensed water path, Panel (e) of the temperature at 500 hPa, and Panel (f) of the zonal wind at 200 hPa as a function of latitude. The plotted values were averaged over both hemispheres.

Although changing convective clustering by changing CF has a substantial effect on the zonal mean meridional variance of water-related quantities (precipitation, water vapor, clouds etc.), it has no clear systematic impact on the zonal variance of these quantities (Figures 5a and 5d).

4.2. Increased Convective Clustering Associated With Fewer Convective Regions

By contrast, increasing convective clustering by decreasing the zonal wavenumber ν and thus the number of convective regions leads to an increase of the zonal variance of water-related quantities in the equatorial region. This is evidenced by the increase in the difference in humidity and in the condensed water path between the convective regions and the subsidence regions with fewer convective regions (Figures 5b and 5d).

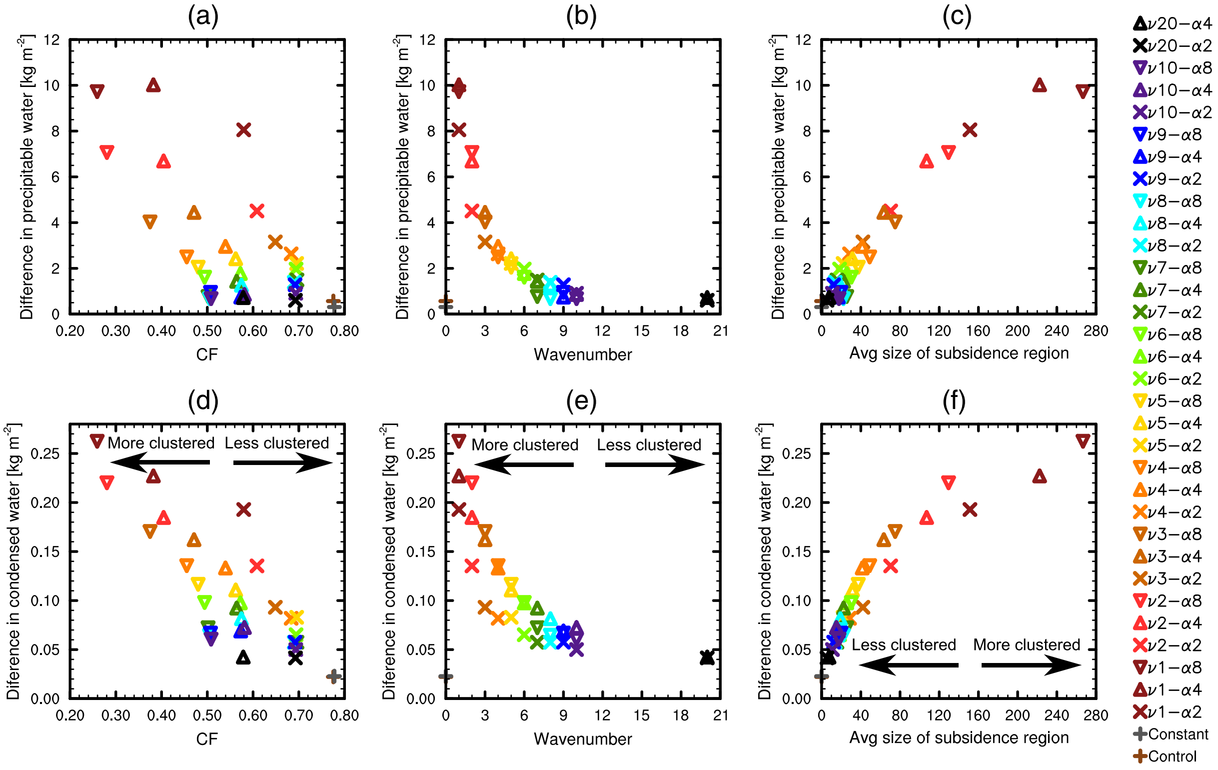

Figure 5. Panel (a) shows the difference in steady-state precipitable water between the convective ($\omega(p = 500\,\text{hPa}) < 0$) and the subsidence ($\omega(p = 500\,\text{hPa}) > 0$) regions in the zonal band between 6°S and 6°N and Panel (d) the difference between these regions in the steady-state condensed water path, both plotted as a function of the convective fraction (CF). Panel (b) shows the same as (a) and Panel (e) as (d) but for the zonal wavenumber instead of the CF, where the CONTROL and CONSTANT experiments are plotted as Wavenumber 0. Panel (c) shows the same as (a), and Panel (f) as (d) but for the average zonal extent of the subsidence region L_D calculated as $360°\cdot(1-\text{CF})/\nu$ and setting CONTROL and CONSTANT to $L_D = 0$.

On the other hand, the impact of increasing convective clustering by decreasing the number of convective regions on the equatorial mean of the water-related quantities is generally weaker than it is for decreasing CF at higher wavenumbers (ν>5; see Figures 6a and 6c and Table 1). Some quantities have a dependence on the number of convective regions at these higher wavenumbers, however, such as the precipitable water or the cloud cover that keeps increasing with the number of convective regions (in particular for the α4 and α8 experiments). The stronger dependence of the equatorial mean of water-related quantities at smaller wavenumber is consistent with the monotonically increasing relationship between the number of convective regions and the CF for $\nu \leq 5$ (Figure 2b) (since these quantities all strongly depend on the CF) and suggests that a substantial effect of the number of convective regions for these lower wavenumbers occurs through its implicit impact via the CF. By removing the implicit impact on these quantities of the number of convective regions through its impact on the CF, we find indeed that the explicit behavior of these quantities at the lower wavenumbers is similar to that at higher wavenumbers (Figures 6b and 6d; see Appendix A for how this is done).

There is no clear impact of the number of convective regions on the tropical mean of most other quantities, implying a compensation of the effects seen in the equatorial region at higher latitudes (Figures 4a–4d). An exception is the zonal mean zonal wind, for which increased convective clustering leads to a substantial acceleration in the upper troposphere (Figure 4f), such that equatorial superrotation is observed for one to four convective regions, as well as for five to seven convective regions in the experiments with smaller CF (Figure 6e).

In summary, increasing convective clustering by decreasing the number of convective regions leads to an increase in the zonal variance of water-related quantities in the equatorial region. It also leads to a small decrease in equatorial mean precipitable water and cloud fraction and to an acceleration of the equatorial

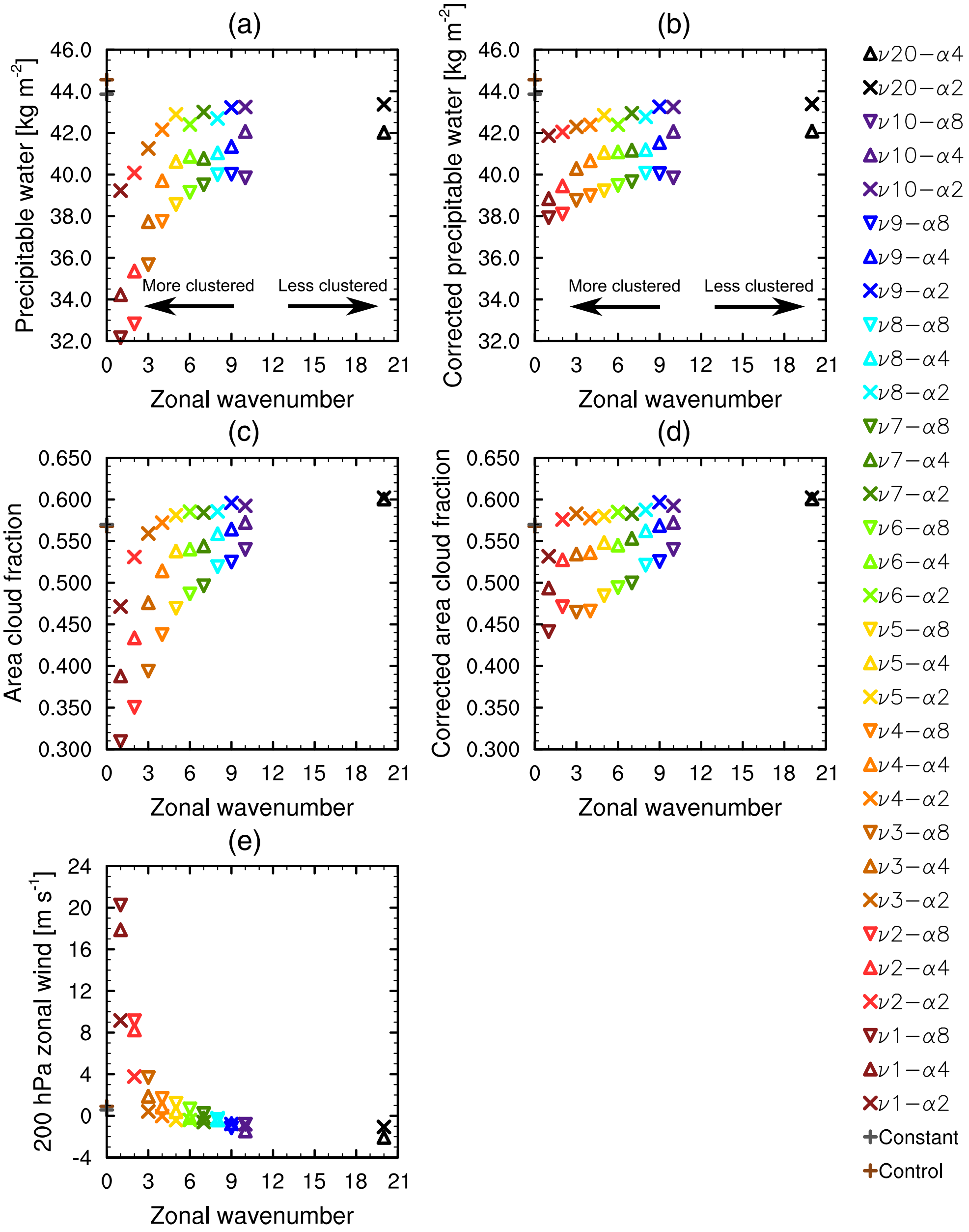

Figure 6. Panel (a) shows the steady-state precipitable water, Panel (c) the steady-state area cloud fraction, and Panel (e) the steady-state zonal wind at the 200 hPa pressure level, all averaged over the zonal band from 6°S to 6°N as a function of the zonal wavenumber ν where the CONTROL and CONSTANT experiments are plotted as Wavenumber 0. Panels (b) and (d) show the corrected steady-state precipitable water and the corrected area cloud fraction, respectively, averaged over the zonal band from 6°S to 6°N as a function of the zonal wavenumber. The steady-state precipitable water and area cloud fraction averaged over the zonal band from 6°S to 6°N were corrected such that the influence on these quantities through the influence of the zonal wavenumber on CF was removed following the methodology described in Appendix A. Note that this correction procedure could not be applied to the zonal wind at 200 hPa, because the zonal wind at 200 hPa does not have a well-defined relationship with CF (not shown).

mean zonal wind. A compensation effect at higher tropical latitudes offsets most of these effects in the tropical mean.

4.3. Decomposition Into Zonal Mean and Zonally Anomalous Climate Impacts of Convective Clustering

Temporal mean changes of climate variables can be decomposed into a contribution from zonal-mean changes and from zonally anomalous changes. We start with the zonal-mean contribution. In contrast to

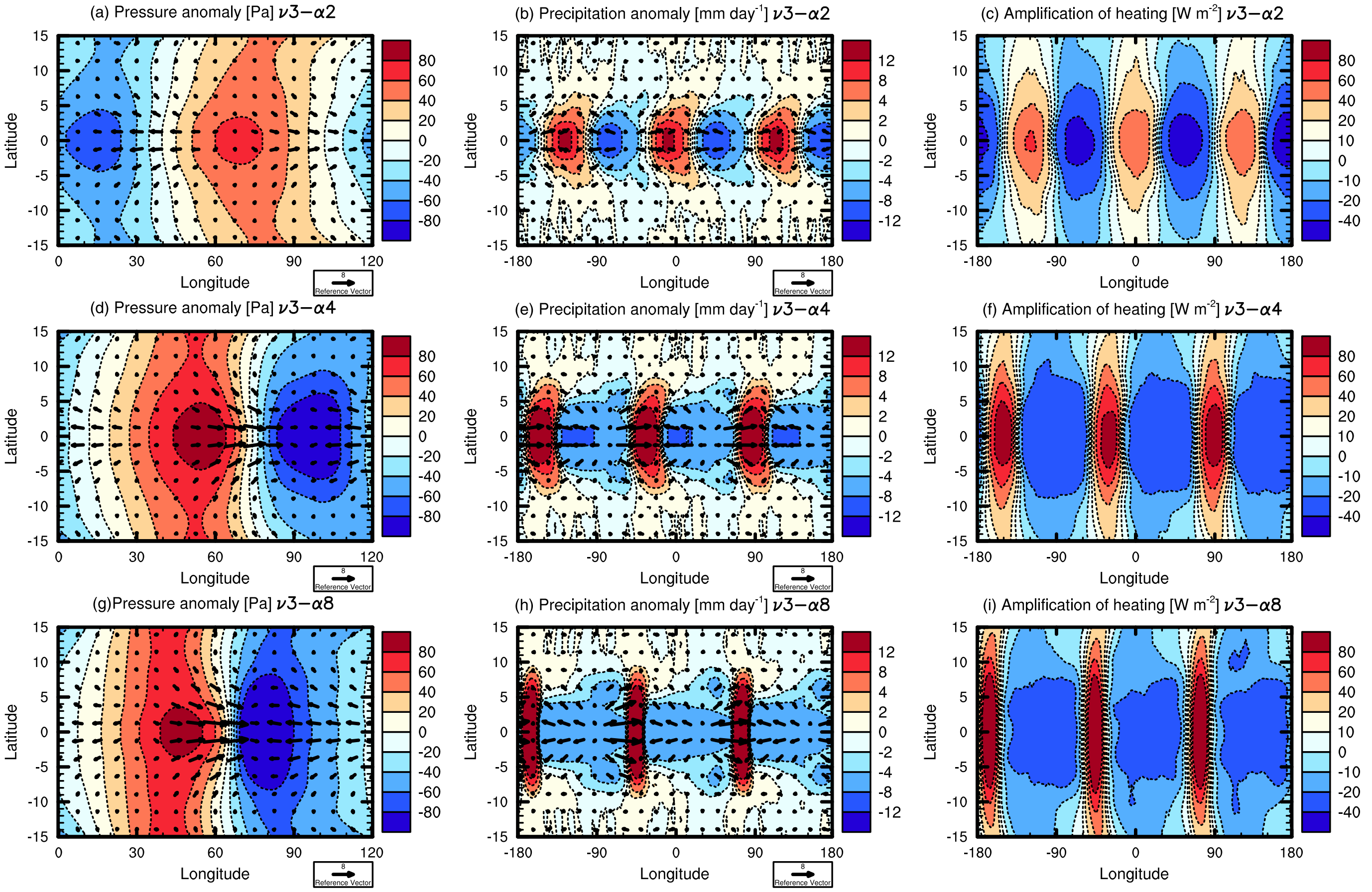

Figure 7. Zonal anomalies of the temporal mean surface pressure and wind vectors in the ν3-α2 (Panel a), ν3-α4 (Panel d), and ν3-α8 (Panel g) experiments. Zonal anomalies in precipitation and wind vectors in the ν3-α2 (Panel b), ν3-α4 (Panel e), and ν3-α8 (Panel h) experiments. The fields in these plots were symmetrized about the equator. Difference in zonal anomalies between the temporal mean atmospheric energy uptake and the imposed latent heat flux in the ν3-α2 (Panel c), ν3-α4 (Panel f), and ν3-α8 (Panel i) experiments. Note that the maxima of evaporation are displaced in longitude in the experiments with different amplitudes, so the regions of strong convection and the subsidence regions are also displaced. The left column only shows longitudes from 0° to 120°, whereas the middle and right column show the entire zonal band.

the equatorial or the tropical mean, the impact of convective clustering on the zonal mean of the water-related variables is far from systematic (Figures 4a–4d). For example, there is a single ITCZ structure in the control simulation, a double ITCZ structure in most other simulations, and even a triple ITCZ structure in a few experiments such as ν1-α8. This highlights how sensitive the meridional structure of zonal mean precipitation is to zonal aspects of the forcing.

Many aspects of the anomalous zonal response to changing the imposed evaporation forcing (and thus convective clustering) can be understood from the large body of work on the tropical atmosphere's response to zonally anomalous heats sources and sinks (e.g., Arnold et al., 2012; Adam, 2018; Adames & Kim, 2016; Gill, 1980; Lutsko, 2018; Matsuno, 1966; Showman & Polvani, 2010; Sobel & Maloney, 2012). This is because changing the evaporation has (through the latent heat flux) also the effect of adding surface heat sources or sinks. The anomalous stationary wave response to the imposed evaporation patterns closely resembles the classic Matsuno-Gill model for the tropical atmosphere's response to imposed heating (Gill, 1980; Matsuno, 1966), with a Kelvin wave to the east of the heating and two Rossby lobes southwest and northwest of the heating, respectively (Figure 7, left and middle columns). The wavenumber ν affects the horizontal scale of the anomalous response (not shown), as would naturally be expected. The amplitude of the imposed evaporation affects the magnitude of the zonally anomalous wind response but does not substantially change its spatial structure. This is because the local convective heating anomalies are amplified by radiative feedbacks (Figure 7, right column): The increased convection over the regions of increased latent heat flux leads to an increase in the atmospheric cloud-radiative effect (defined as the difference between the total net [LW + SW] top of the atmosphere minus the total net surface radiative flux and the clear-sky net top of the atmosphere minus the clear-sky net surface radiative flux), whereas the suppressed convection in the regions of reduced latent heat flux leads to a decrease in the atmospheric cloud-radiative effect. This implies that changing the convective clustering (through changing either the CF or the number of convective regions) by itself causes an anomalous response that is similar to the anomalous response analyzed here, regardless of what causes the convective clustering.

5. Mechanisms for the Impacts of Convective Clustering on the Tropical Moisture Distribution

5.1. Mechanisms for the Impact of the Convective Fraction

A mechanism for the impact of the convective fraction on the width of the ITCZ was suggested by PB19. We repeat the argument here then test its validity in sensitivity experiments. PB19 suggest that reducing CF (according to their precipitation-based metric that is equivalent to CF) leads to a decrease in atmospheric cloud-radiative effect in the equatorial region (see their Figure 6, and Figure 8b of this manuscript). This leads to a decrease in the meridional gradient of atmospheric energy uptake, which in turn leads to a weakening of the meridional circulation (see their Figure 6, and Figure 8c of this manuscript) and hence a reduced transport of water toward the equator. Since the zonal mean evaporation is held approximately fixed in the simulations, a reduction in meridional water vapor transport leads to a reduction in near-equatorial precipitation and to an increase in precipitation at poleward tropical latitudes in steady state and thus to a wider ITCZ (see, e.g., Figure 8a). In principle these arguments also explain the wider meridional distribution of other water-related quantities in the analyzed simulations for smaller CF (Figures 4c and 4d).

In order to test how well the mechanism suggested by PB19 explains the impact of the CF on the width of the ITCZ, we perform sensitivity experiments in which we turn off all interactions between clouds and radiation; that is, we make clouds transparent to radiation. We find that the regression coefficient from the width of the ITCZ onto CF is reduced by 37% when the cloud-radiative interactions are turned off, suggesting a weaker relation between the two variables in this case (Figure 8a). This confirms that the atmospheric cloud-radiative effect explains a substantial part of the impact of CF on the width of the ITCZ.

However, even if the relationship is weaker, a reduction of the convective fraction is still associated with a wider ITCZ in the experiments with no interactions between clouds and radiation (Figure 8a). So where is the remaining effect coming from? To investigate this, we use a gross moist stability (GMS) framework. This framework allows us to link the intensity of the meridional overturning circulation to the atmospheric energy budget. In a hemispherically symmetric configuration such as the aquaplanet simulations analyzed here, this framework allows us to express the strength of the Hadley circulation $\Psi_{\max}(\phi)$ as (see PB19 for a derivation)

$$\Psi_{\max}(\phi) = \frac{A(\phi)\overline{H_{\mathrm{a}}}^{[0,\,\phi],\,t}}{\overline{\Delta h(\phi)}^{\,t}}, \tag{1}$$

where ϕ denotes the latitude, A the area between the equator and latitude ϕ, H_{a} the atmospheric energy uptake, t time, $[0, \phi]$ the zonal band between the equator and latitude ϕ, and $\overline{\cdot}$ the average over the quantities denoted on the top right. $\overline{\Delta h(\phi)}^{\,t}$ is the GMS that gives the framework its name and is defined here as

$$\overline{\Delta h(\phi)}^{\,t} = \frac{\left\langle \overline{h(\phi)v(\phi)}^{\,\lambda,\,t} \right\rangle_{\mathrm{p}}}{\left\langle \overline{v(\phi)}^{\,\lambda,\,t} \right\rangle_{\mathrm{p_m}}}, \tag{2}$$

where v denotes the meridional wind, λ the longitude, $\langle \cdot \rangle_{\mathrm{p_m}}$ denotes the mass weighted vertical integral from the top of the atmosphere to a "midlevel" $\mathrm{p_m}$ where the meridional wind changes direction, and $\langle \cdot \rangle_{\mathrm{p}}$ denotes the mass weighted vertical integral over the entire atmosphere. h denotes the frozen MSE defined as

$$h = c_{\mathrm{p}}T + gz + Lq - L_{\mathrm{f}}q_{\mathrm{i}}, \tag{3}$$

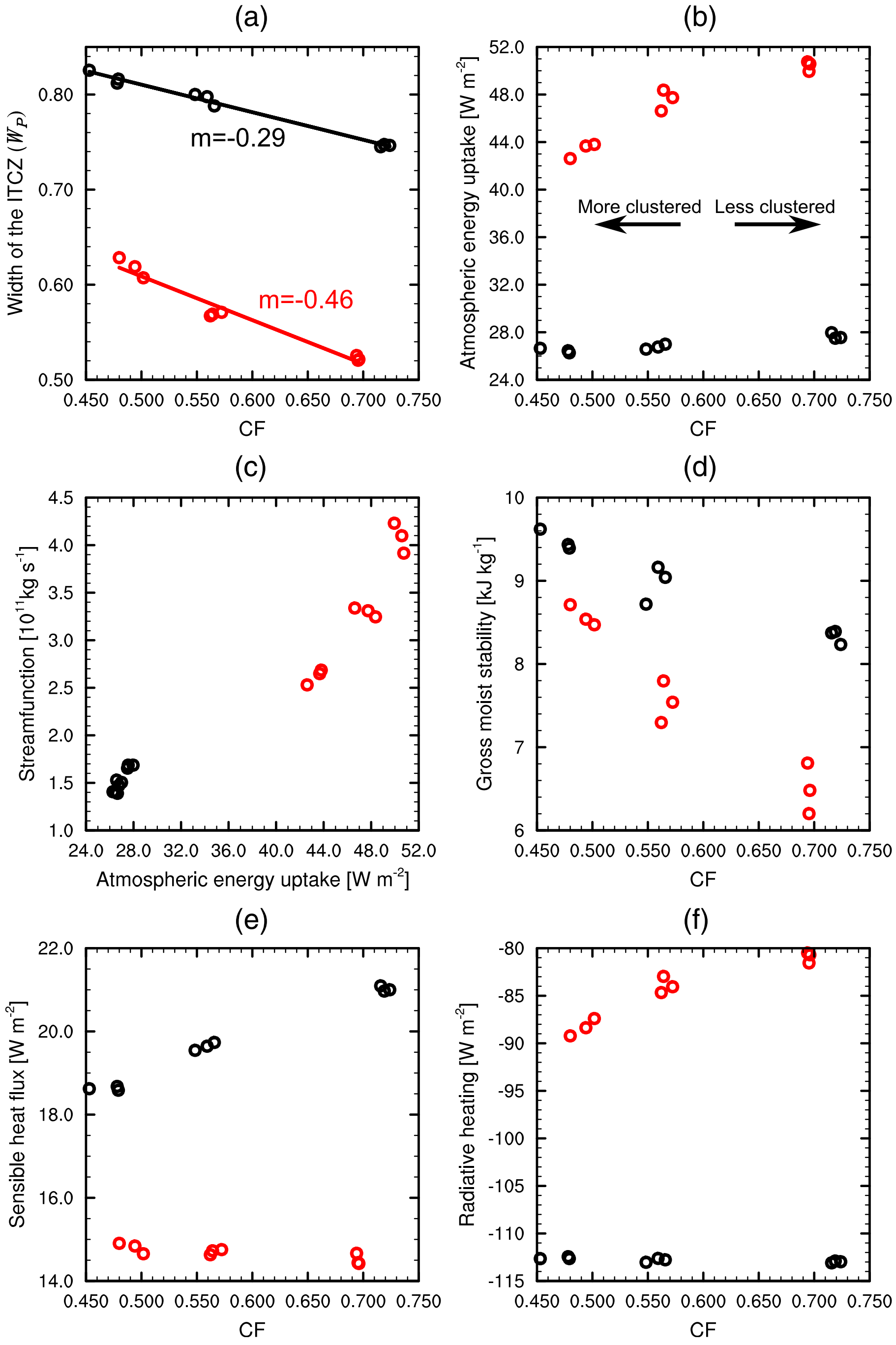

Figure 8. Panel (a) shows the precipitation-inferred width of the ITCZ (W_P), Panel (b) shows the area mean from 6°S to 6°N of the net atmospheric energy uptake, Panel (d) of the gross moist stability, Panel (e) of the sensible heat flux, and Panel (f) of the vertically integrated radiative heating as a function of CF in steady state. The precipitation-inferred width of the ITCZ is calculated by taking the mean precipitation of the zonal band from 15°S to 15°N and dividing it by the mean precipitation of the zonal band from 6°S to 6°N. Panel (c) shows the absolute value of the Eularian mean mass streamfunction at 500 hPa averaged from 6°S to 6°N as a function of the net atmospheric energy uptake. Black marks correspond to the steady-state value of the experiments with zonal Wavenumbers 5 through 7 and $\alpha = 2$, 4, and 8 in the experiments with the atmospheric cloud-radiative effects turned off and red marks from the corresponding experiments with the atmospheric cloud-radiative effects turned on. The regression lines were added to Panel (a) for the cases with and without cloud-radiative effects with their respective slopes (m).

where c_p is the specific heat capacity of air at constant pressure, T the temperature, g Earth's gravity acceleration, z the height above sea level, L the latent energy of vaporization, L_f the latent heat of fusion, q the specific humidity, and q_i the specific mass of ice.

Equation 2 indicates that the GMS can be interpreted as the meridional energy advection divided by the mass flux in the upper branch of the Hadley circulation and thus corresponds to the efficiency with which the Hadley circulation transports this energy away meridionally. With this interpretation, Equation 1 states that the strength of the Hadley circulation at a given latitude ϕ corresponds to the integrated energy uptake over the total area at lower latitude than ϕ, divided by the efficiency of the Hadley circulation to transport this energy away. Note that if the GMS is small and thus the Hadley circulation inefficient at transporting energy, changes in the atmospheric energy budget will require a large response of the Hadley circulation to restore the energy balance.

This GMS framework helps interpret the clear-sky simulations. In principle there are two ways to weaken the Hadley circulation: either by decreasing the atmospheric energy uptake or by increasing the GMS. We find that the change in equatorial energy uptake with CF is substantially smaller in the clear-sky simulations than in the simulations with the cloud-radiative interactions turned on (Figure 8b). The small decrease in energy uptake with decreasing CF in the clear-sky simulations comes exclusively from the sensible heat flux (Figure 8e). However, since this behavior is not present in the simulations with the atmospheric cloud-radiative effect turned on, it is unlikely that the change in turbulent heat flux is driving the changes in ITCZ properties in the simulations without cloud-radiative effects. Hence, the response of the ITCZ to changes in CF must be driven by changes in the GMS. We find indeed an increase in GMS with decreasing CF (Figure 8d). This is not only the case in the clear-sky simulations but also in the simulations with the cloud-radiative effects turned on, further emphasizing the crucial role of GMS changes.

In order to better understand the origin of the changes in GMS, we decompose the GMS into a temporal mean and a transient component

$$\begin{aligned}\overline{\Delta h(\phi)}^{t} &= \frac{\left\langle \overline{h(\phi)v(\phi)}^{\lambda,t}\right\rangle_{p}}{\left\langle \overline{v(\phi)}^{\lambda,t}\right\rangle_{p_m}}\\ &= \underbrace{\frac{\left\langle \overline{\overline{h(\phi)}^{t}\,\overline{v(\phi)}^{t}}^{\lambda}\right\rangle_{p}}{\left\langle \overline{v(\phi)}^{\lambda,t}\right\rangle_{p_m}}}_{\text{temporal mean}} + \underbrace{\frac{\left\langle \overline{h(\phi)'v(\phi)'}^{\lambda,t}\right\rangle_{p}}{\left\langle \overline{v(\phi)}^{\lambda,t}\right\rangle_{p_m}}}_{\text{transient}},\end{aligned} \tag{4}$$

where primes denote departures from temporal means. We find that the increase in GMS with decreasing CF comes from the temporal mean component (compare Figures 9a and 9c). We hence decompose the temporal mean change in GMS further into a component from changes in the frozen MSE (h) and into a component from changes in the vertical profiles of the meridional wind v. We find that the main change in mean GMS comes from changes in the vertical profiles of the meridional wind (compare Figures 9c and 9d).

Changes in the vertical profiles of the meridional wind affect the GMS by changing the levels at which mass convergence and divergence occur, thus changing the energy density of the mass that is replaced. Owing to the continuity equation, the zonal mean meridional mass convergence is equal in magnitude but opposite in sign to the zonal mean vertical mass convergence. Therefore, in order to analyze how the levels of mass convergence and divergence affect the GMS, we can also analyze the vertical wind profiles (which has been the more frequently used methodology in the past). The vertical wind profiles become increasingly top-heavy when convective clustering is increased by decreasing CF (by increasing α), and therefore the vertical distribution of horizontal mass divergence becomes more top-heavy as well (Figures 10a and 10b). As a consequence, air of higher MSE is exported and air of lower MSE is imported (Back & Bretherton, 2006; Inoue & Back, 2015) thus increasing the energy transported poleward per unit of circulated mass and hence increasing the GMS. The vertical wind profiles in the simulations become more top-heavy with convective clustering through decreasing CF, because the contribution of the vertical mass flux from strong

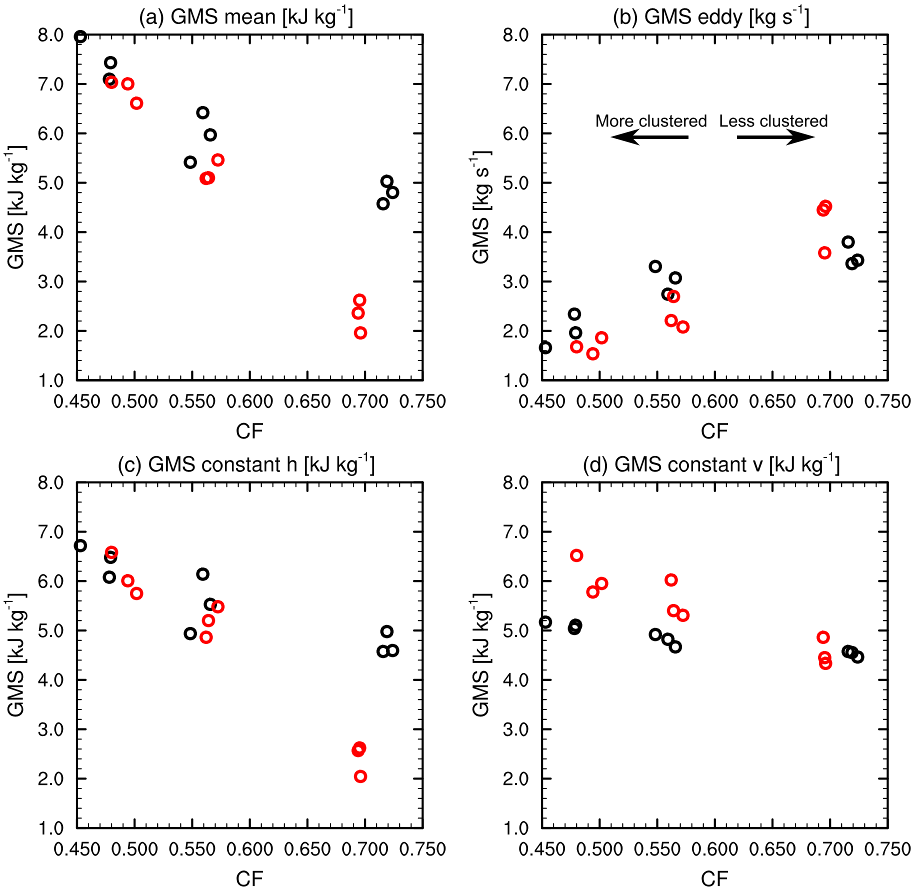

Figure 9. Panel (a) shows the steady-state gross moist stability (GMS) inferred from the stationary circulation averaged from 6°S to 6°N. Panel (b) shows the eddy component of the GMS calculated as the difference of the net GMS and the GMS calculated from the stationary circulation. Panel (c) shows the same as Panel (a) assuming that the frozen moist static energy is the same as the one from the $\nu5$-$\alpha2$ experiment in all experiments. Panel (d) shows the same as Panel (a) assuming that the poleward wind component is the same as the one from the $\nu5$-$\alpha2$ experiment in all experiments. Black marks correspond to the steady-state value of the experiments with zonal Wavenumbers 5 through 7 and $\alpha = 2$, 4, and 8 in the experiments with the atmospheric cloud-radiative effects turned off and red marks from the corresponding experiments with the atmospheric cloud-radiative effects turned on.

convective events increases with decreasing CF (the contribution to the vertical mass flux from strong convective events with $\omega<200$ hPa day^{-1} at 400 hPa increases from 0.7% in the $\alpha2$ experiments to 48.2% in the $\alpha8$ experiments) and because the wind profiles of strong convective events are more top-heavy (Figures 10c and 10d). Note that a tendency to stronger convective events with decreased CF is consistent with the drier conditions found in the ascent (and subsidence) regions with decreased CF, as more instability needs to build up to trigger deep convection.

In summary, we find an additional mechanism acting in the same direction as the one proposed by PB19: If CF decreases and thus convective clustering increases, the increasing contribution of strong convective events to the upward mass flux increases, resulting in a more top-heavy vertical wind profile that leads to an increase in GMS. This increase in GMS then leads to a weakening of the mean meridional circulation and thus to a widening of the ITCZ.

5.2. Mechanisms for the Impact of the Number of Convective Regions

Varying the zonal wavenumber of the imposed evaporation pattern changes the average zonal extent of the subsidence regions in the deep tropics. The distance between the centers of the dry regions and the convective regions increase with decreasing zonal wavenumber and thus with increasing convective clustering. This distance corresponds (by design) to half the average zonal extent of the subsidence regions, which we

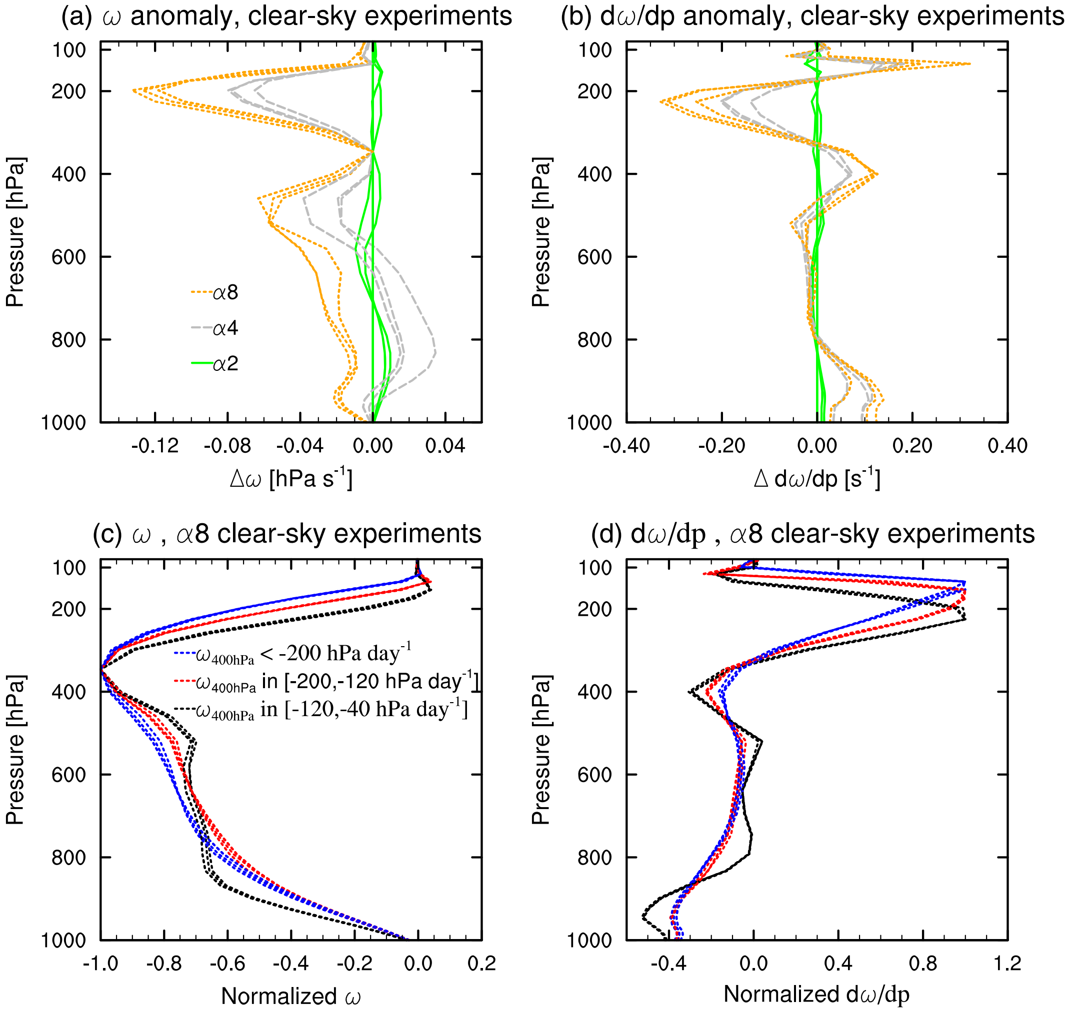

Figure 10. Panel (a) shows the anomaly relative to the $\nu5$-$\alpha2$ experiment ($\Delta\omega = \omega(\text{experiment}) - \omega(\nu5-\alpha2)$) of the area mean from 6°S to 6°N of the steady-state vertical pressure velocity profiles (ω) and Panel (b) of the derivative with respect to pressure thereof ($d\omega/dp$) for the clear-sky experiments with Wavenumbers 5 through 7 and $\alpha = 2$ (solid lines, green), 4 (dashed lines, gray), and 8 (dotted lines, orange). Panel (c) shows the vertical profiles of ω and Panel (d) of $d\omega/dp$ averaged over the zonal band from 6°S to 6°N in the $\alpha8$ experiments for different convective regimes. The black dotted lines show the average for events where ω at 400 hPa is between -120 and -40 hPa day^{-1}, the red dotted lines where it is between -200 and -120 hPa day^{-1}, and the blue dotted lines where it is smaller than -200 hPa day^{-1}. Note that by mass conservation, $d\omega/dp$ is proportional to the horizontal mass divergence. $d\omega/dp$ and ω were normalized by dividing by the maximum of the respective value for each experiment. The legends in Panels (a) and (b) indicate the dash pattern and color associated with each amplitude. In Panels (c) and (d) they indicate from what interval of ω the average was calculated.

denote by L_D. This average zonal extent of the subsidence regions is largely responsible for the influence of the wavenumber on the deep tropical climate as we will show in this section. We diagnose L_D as the subsidence fraction ($1 - \text{CF}$) divided by the zonal wavenumber ν multiplied by 360°:

$$L_D = 360\,° \cdot \frac{1 - \text{CF}}{\nu}. \tag{5}$$

We note that the dependence of L_D on CF is a consequence of the zonal shape of evaporation patterns that we chose and is not in this sense of physical origin.

Moisture enters the free troposphere predominantly in regions of deep convection and is then propagated into the subsidence regions by detraining anvil clouds (e.g., Emanuel & Živković-Rothman, 1999;

Pierrehumbert, 1998; Romps, 2014; Sherwood et al., 2010). So the further away a point lies from the closest convective region, the drier it is. This implies that increasing the size of subsidence regions and thus L_D should decrease the atmospheric moisture content and increase the zonal variance thereof (Figures 5c, 11a, and 11b). Since L_D increases when the number of convective regions is decreased, we find similar relationships when decreasing the number of convective regions (Figures 5b, 6a, and 6b). Similarly, one should also expect the high cloud fraction to decrease and its zonal variance to increase with increasing L_D (Figures 5e, 11c, 11d) (and thus decreasing number of convective regions [Figures 5e, 5f, 6c, and 6d]), as a larger L_D means that a smaller fraction of each subsidence region will be covered by high clouds. This argument also explains why the impact of convective clustering, measured by the number of convective regions, on the tropical climate becomes more pronounced when there is a relatively small number of convective regions: As shown in Equation 5, the average size of the subsidence region should be roughly inversely proportional to the imposed number of convective regions, implying that the rate of decrease of the size of the subsidence regions increases with a decreasing number of convective regions. By plotting the aforementioned water-related quantities as a function of L_D, we find indeed a more linear behavior (Figures 5c, 5f, and 11a–11d and Table 1).

L_D also has a nearly perfect linear relationship with the zonal mean zonal wind at 200 hPa (Figure 11e). It is, however, not intuitively clear why the zonal mean zonal wind should accelerate as the average size of the subsidence regions is increased. An analysis of the zonal mean zonal momentum budget indicates that the acceleration is driven by the increased stationary eddy momentum fluxes (not shown) as L_D is increased (i.e., as ν is decreased). This suggests that either the meridional propagation of the waves excited by the evaporation patches depends on L_D and/or that the stationary wave source depends on L_D, but investigating this further is beyond the scope of the present study.

In summary, most of the relationships with the number of convective regions can be explained by the average size of subsidence regions (L_D): The larger the subsidence areas, the drier the atmosphere. We therefore believe that metrics that characterize the size distribution of the subsidence regions would be particularly well suited for characterizing the effects of altering the spatial distribution of convection.

6. Discussion

6.1. Comparison to Other Metrics of Convective Clustering

A number of different metrics have been used in the past to characterize convective clustering. Some of them require high spatial or temporal resolutions or a large number of grid points, such as index of organization I_{org} (Tompkins & Semie, 2016), the simple convective aggregation index (SCAI) (Tobin et al., 2012), or the convective aggregation index (CAI) (Pendergrass et al., 2016), that are not available for the analyzed GCM results and hence cannot be applied. Other metrics, however, can readily be applied to our results. These are the subsidence fraction (Coppin & Bony, 2015), the interquartile ratio of precipitable water (IQR Bretherton et al., 2005), and the normalized zonal standard deviation of precipitation ($\overline{S_\lambda(P)}$; PB19).

The subsidence fraction SF is the fractional area of mean subsidence (i.e., $\omega(500\,\text{hPa}) > 0$) and is almost equal to $1 - \text{CF}$ except for a small detail in the manner we calculate CF: CF is calculated by taking the meridional average from 6°S to 6°N first and by then taking CF to be the zonal fraction of values of $\omega(500\,\text{hPa}) < 0$. For SF to be identical to $1 - \text{CF}$, we would have to calculate CF as the actual area fraction with $\omega(500\,\text{hPa}) < 0$ in the zonal band from 6°S to 6°N (so without taking the meridional average first). However, the two ways of calculating CF are very highly correlated (95% of the variance explained) and thus characterize the same aspect of convective clustering. Thus, relationships with SF are equivalent to relationships with CF (but with opposite sign).

The normalized zonal standard deviation of precipitation is also very closely tied to CF, with higher values of the zonal standard deviation of precipitation corresponding to more clustered states (Figure 2c). The zonal standard deviation of precipitation increases with decreasing wavenumber (Figure 2d), but only at low wavenumbers, and thus shows a similar behavior as CF in this regard.

The IQR has been used as a metric for convective clustering in RCE simulations, where it was found that the horizontal variability in humidity increases as the convective clustering increases (Bretherton et al., 2005).

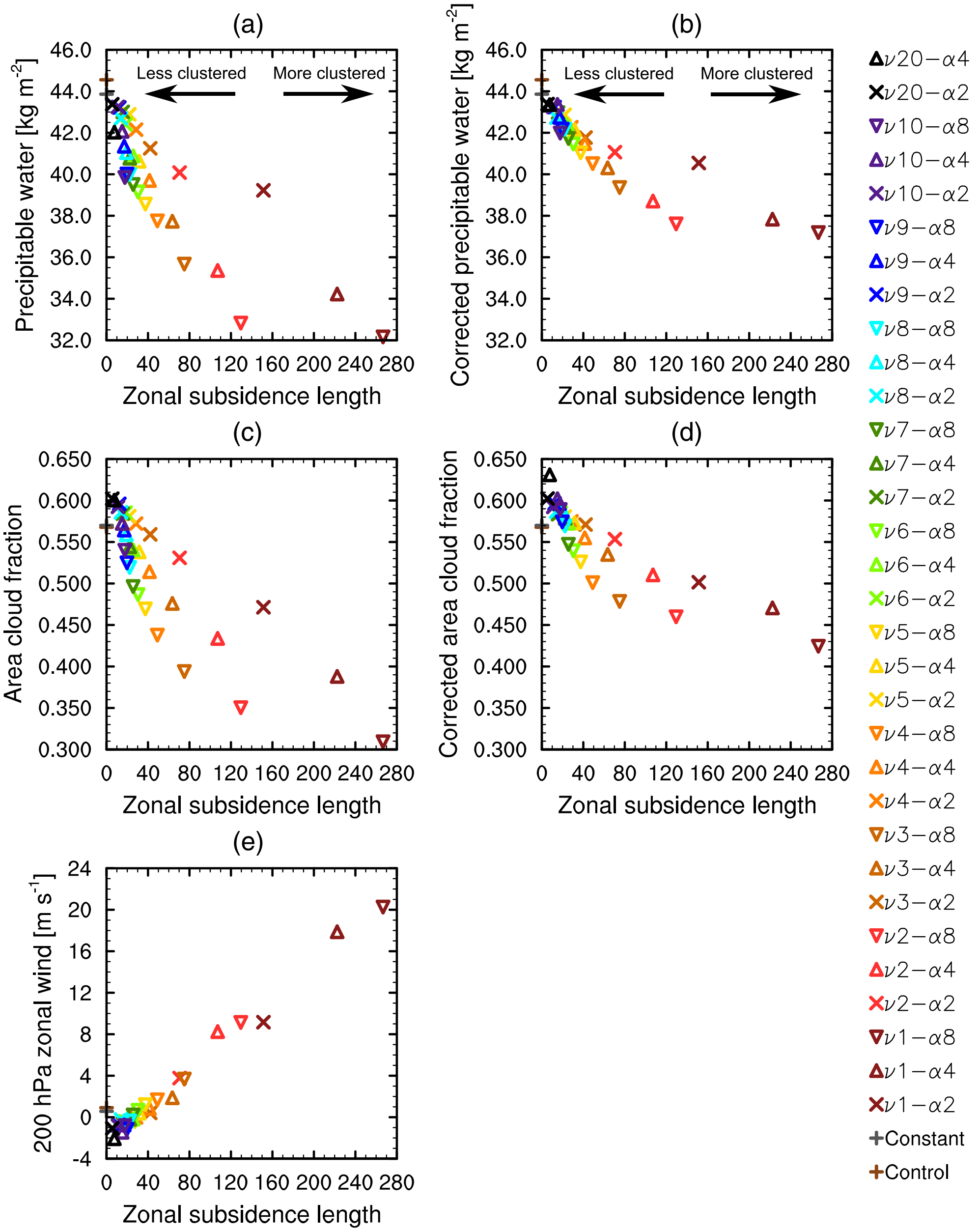

Figure 11. Panel (a) shows the steady-state precipitable water, Panel (c) the steady-state area cloud fraction, and Panel (e) the steady-state zonal wind at the 200 hPa pressure level, all averaged over the zonal band from 6°S to 6°N, as a function of the average zonal extent of the subsidence region L_D calculated as 360°·(1−CF)/ν and setting CONTROL and CONSTANT to $L_D = 0$. Panels (b) and (d) show the corrected steady-state precipitable water and the corrected area cloud fraction, respectively, averaged over the zonal band from 6°S to 6°N as a function of L_D. The steady-state precipitable water and area cloud fraction averaged over the zonal band from 6°S to 6°N were corrected such that the influence on these quantities through the influence of L_D on CF was removed following the methodology described in Appendix B. Note that this correction procedure could not be applied to the zonal wind at 200 hPa, because the zonal wind at 200 hPa does not have a well-defined relationship with CF (not shown).

The IQR increases monotonically with decreasing zonal wavenumber (and hence increasing convective clustering), but there is no clear relationship with the CF (Figures 2e and 2f).

In summary, the subsidence fraction and the normalized zonal standard deviation of precipitation describe the same quality of convective clustering as the CF, and the IQR describes the same quality of convective clustering as the zonal wavenumber or the mean zonal extent of the subsidence zones.

6.2. Comparison Between the Aquaplanet Results and Previous Results Obtained in RCE Simulations

In this section we focus on similarities between the aquaplanet results and RCE simulations, particularly by comparing the aquaplanet results with features that are robustly seen in RCE simulations.

The results of the aquaplanet simulations agree with most robust RCE results, such as stronger convective clustering (either by changing CF or by changing the number of convective regions) being associated with drying, a reduction of cloud cover, a decreased cloud-radiative effect, and an increase in the IQR in the region where the clustering is imposed (Bretherton et al., 2005; C. Muller & Bony, 2015; Wing & Cronin, 2016; Wing et al., 2017). The only major difference is that, in the aquaplanet simulations, stronger convective clustering (through changing CF) is associated with a cooling of the troposphere, whereas it is associated with a warming of the free troposphere in RCE with prescribed sea surface temperatures (Wing et al., 2017). This cooling is caused by changes in cloud-radiative effects, as the cooling is not present in the simulations with cloud-radiative interactions turned off (not shown). In the simulations with clouds interacting with radiation, we find that both the equatorial and the tropical fraction covered by high clouds decreases with decreasing CF, leading to higher infrared cooling of the troposphere which should lead to lower tropospheric temperatures (e.g., Slingo & Slingo, 1988). Whether the cloud-radiative interaction are turned on or off, we find robustly that the convective regions themselves also become drier in the aquaplanet simulations with increasing convective clustering by decreasing CF. By contrast, the convective regions tend to become more moist in RCE simulations with convective clustering (Wing et al., 2017). We speculate here that this is due to the enhanced mixing by the circulation between the dry and the moist regions and to the overall drying of the equatorial region associated with the weaker Hadley circulation with decreasing CF that imports less moisture from higher latitudes. As the expanding subsidence regions become drier with decreasing CF, drier air is mixed into the convective regions reducing humidity there as well.

The aquaplanet simulation results suggest furthermore that in RCE the effects of the convective clustering are caused by two different aspects of the convective clustering: the change in area fraction covered by convection, which primarily affects the humidity and cloud-radiative effects, and the size of the subsiding regions, which primarily affects IQR. In RCE simulations the convective fraction tends to decrease simultaneously with increasing size of the subsidence regions, and the individual impacts of the two changes are thus difficult to disentangle. The aquaplanet simulations analyzed here demonstrate that at least two metrics are required for a comprehensive description of the effects of convective clustering on the climate in more realistic configurations. The aquaplanet simulations also reveal that many effects associated with convective clustering in the equatorial region are countered in adjacent regions such that they are substantially reduced in the tropical mean. The impact of convective clustering on the equatorial and tropical climate from changing the convective fraction is generally larger than the one from changing the number of convective regions. This suggests that quantities that characterize convective clustering using the spatial variance of moisture or MSE (that are more closely linked to the size of the subsidence regions) may not be good predictors of the main effects of the clustering (e.g., drying or reduction of cloud-radiative heating).

An additional insight from the aquaplanet simulations comes from breaking the horizontal isotropy of the RCE boundary conditions. The meridional width of the ITCZ can in principle be seen as a metric of meridional convective clustering. According to this metric, a narrower ITCZ corresponds to a more clustered state. This perspective allows us to interpret the result that the ITCZ widens with decreasing CF (which is a metric for zonal clustering) in the following way: Increased zonal convective clustering is associated with reduced meridional convective clustering. This not only suggests that meridional and zonal convective clustering may have distinct impacts on the climate in realistic configurations but also that meridional and zonal convective clustering may act as antagonists.

6.3. Limitations of the Employed Setup and Outlook

A limitation of our setup is that the surface temperatures are fixed and do not respond to imbalances in the surface energy budget. This constrains the responses to the imposed forcing. We find, for example, a difference of up to 0.1 in the equatorial planetary albedo between experiments, with lower values when the CF is smaller. This would severely impact the surface, as the equatorial sea surface would warm when the albedo diminishes. This would in turn lead to an increase in meridional surface temperature gradient, which would strengthen the mean meridional circulation (Bellon & Sobel, 2010; Gastineau et al., 2011; Oueslati & Bellon, 2013) and thus offset at least part of the weakening of the mean meridional circulation found here. This could in turn be offset somewhat by changes in the longwave surface fluxes that would act to amplify the results found here (Fläschner et al., 2018; Harrop & Hartmann, 2016; Popp & Silvers 2017). RCE simulations with interactive sea surface temperatures suggest furthermore that the deep convective regions would not be stationary but would migrate toward local maxima of sea surface temperature and eventually disappear there, before new convective systems form (Coppin & Bony, 2017), thus changing the convective clustering over time. In summary, performing similar simulations to the ones analyzed here but with interactive sea surface temperature is an important next step for understanding how surface feedbacks affect the results found here.

Similarly, forcing evaporation to prescribed patterns also has a variety of implications that could affect the results. Evaporation feedbacks, such as the wind-induced surface heat exchange (WISHE) feedback (Emanuel, 1987; Neelin et al., 1987) that could affect the net input of energy and moisture into the atmosphere and thus change the circulation response, are strongly suppressed in the equatorial region. Due to the coupling of the evaporation to the surface winds and thus to the large-scale circulation, it is not intuitively clear how fixing the evaporation affects the results, and it is thus certainly worth investigating this in the future.

Observations suggest that convective clustering can occur at scales as small as a few kilometers. The limited resolution of the employed GCM impeded us from analyzing the impact of this small-scale convective clustering on the climate. The main open questions in this regard are whether there are impacts of the convective clustering that are substantially different than at the larger scales analyzed here and whether the effect of the sizes of the subsidence region saturates at sufficiently small length scales. Since resolving the smallest scales of convective clustering globally is beyond the capability of current climate models, a useful next step would be to investigate the impact of small-scale convective clustering on the tropical large-scale circulation and climate with high-resolution observational products.

In the experiments analyzed here, the rain belt is confined to the equatorial region. But on Earth the mean position of the rain belt is north of the equator, and it can migrate substantially away from the equator due to the seasonal cycle (Gruber, 1972; Popp & Lutsko 2017; Schneider et al., 2014; Waliser & Gautier, 1993). Furthermore, recent work suggests that the coupling of deep convection to the large-scale circulation is different off the equator (Adames & Ming, 2018a, 2018b), and therefore convective clustering may have a different impact on convection off the equator than near the equator. Since convective clustering has an impact on the energy budget as evidenced here and in observations (Tobin et al., 2012, 2013), and since the atmospheric energy budget has been shown to have a substantial impact on the position of the rain belt (e.g., Adam et al., 2016; Hwang & Frierson, 2013; Kang et al., 2008; Schneider et al., 2014; Wei & Bordoni, 2018), it also seems likely that the position of the rain belt is affected by convective clustering. Studying the interaction between the convective clustering and the rain belt migrations will thus be an important extension to the present study.

Analyses of transient aspects of the aquaplanet simulation results such as transient waves, possible modes of climate variability, or extreme value statistics are also potentially rewarding topics for future studies (Pendergrass et al., 2016; Pendergrass, 2020; Semie & Bony, 2020).

7. Summary

In this study, we have analyzed a set of idealized aquaplanet simulations, first described in Popp and Bony (2019), in which different forms of zonal convective clustering are imposed in the equatorial region. This setup has two free parameters which control the nature of the convective clustering: the fraction of the area covered by convection and the number of convective regions, allowing us to investigate how different forms of convective aggregation can affect the tropical climate.

As shown by Popp and Bony (2019), a shrinking of the convective fraction is associated with reduced cloud-radiative heating and thus a reduction of total atmospheric energy uptake in the deep tropics. This leads to a reduction of the meridional gradients in the atmospheric energy uptake, which in turn leads to a weakening of the large-scale circulation. As a consequence, meridional gradients of precipitation and other water-related quantities decrease. The shrinking of convective areas is also associated with a cooling of the entire tropical atmosphere, due to increased longwave emission to space owing to the reduced area fraction that is covered by cloud anvils. New experiments in which clouds are made transparent to radiation suggest that the aforementioned impacts on the climate result partly from reduced cloud-radiative effects. A second, new effect is associated with increased GMS with decreasing convective fraction, which is attributed to a higher contribution to the total vertical mass flux by strong convective events with top-heavy vertical wind profiles.

The number of convective regions affects the climate mostly by changing the size of subsidence regions in between convective areas, with the subsiding regions expanding as the number of convective regions decreases. Regions within the subsidence areas tend to be further away from convective regions (which are the main source of water in the free troposphere of the subsidence regions), and therefore the subsidence regions tend to be drier and the spatial variance of water higher when the subsidence regions are large. A larger distance between the subsidence and the convective regions is also associated with an (eastward) acceleration of the upper tropospheric winds and for sufficiently small wavenumbers, strong equatorial superrotation.

The zonally anomalous wind response to imposed evaporation patterns exhibits a typical Matsuno-Gill-type pattern, with anomalous easterlies (westerlies) to the east (west) of the areas of maximum evaporation (positive heating anomalies) and meridional divergence (convergence) to the east (west). The reason why the anomalous response follows so closely the spatial patterns from linear theory is that the atmospheric response amplifies the imposed heating patterns by increasing the cloud-radiative heating over the regions of increased evaporation (positive heating anomalies) and doing the opposite over the regions of suppressed evaporation (negative heating anomalies), thereby conserving the localization of heating and cooling. This suggests that the heating patterns caused by convective clustering would have the same spatial pattern even if they were forced differently or would develop spontaneously as a result of self-organization.

Overall, the convective clustering in the aquaplanet simulations presents many similarities with clustering in RCE simulations, but there are also several distinct differences. For instance, increasing convective clustering is not necessarily associated with a warming of the troposphere in the simulations analyzed here but is associated with a cooling when the total convective fraction is decreased. Furthermore, there is no systematic change in the spatial variance of water vapor with the convective fraction, as has been found in RCE simulations. The distinct differences in the respective impacts of the size of the individual subsidence regions and of the total convective fraction suggests that the overall impact of convective clustering on the domain climate found in RCE is a combination of both effects and that using at least two metrics to characterize convective clustering in more realistic settings would be insightful.

Appendix A: Removing the Implicit Impact of the Zonal Wavenumber Through Its Effect on the Convective Fraction

We suspect that some of the impacts of the number of convective regions on certain variables, such as the equatorial mean precipitable water or the area cloud fraction, occur through the relation between the number of convective regions and the convective fraction. However, we would like to know what the relation between the number of convective regions and these variables is, if in our setup the number of convective regions and the convective fraction were independent. Mathematically, this problem can be described as follows. Let ν be the zonal wavenumber of the imposed evaporation forcing and hence the number of convective regions, c the convective fraction, and f a variable that depends on ν and c. The convective fraction furthermore depends on the amplitude of the evaporation forcing α. By design of our experiment ν is independent of α. The change of f with ν in our problem is

$$\frac{df(c(\nu,\alpha),\nu)}{d\nu} = \frac{\partial f(c(\nu,\alpha),\nu)}{\partial c} \cdot \frac{dc(\nu,\alpha)}{\partial \nu} + \frac{\partial f(c(\nu,\alpha),\nu)}{\partial \nu}. \quad \text{(A1)}$$

In this equation, the first term on the right-hand side describes how the wavenumber affects f through its effect on the convective fraction, and the second term describes how the wavenumber affects f directly (explicit effect). Note that when we take the partial derivative of f with respect to ν, we assume that c is held constant. We would like to extract the second term, which can be done by rearranging Equation A1:

$$\frac{\partial f(c(\nu,\alpha),\nu)}{\partial \nu}=\frac{df(c(\nu,\alpha),\nu)}{d\nu}-\frac{\partial f(c(\nu,\alpha),\nu)}{\partial c}\cdot\frac{dc(\nu,\alpha)}{d\nu}. \tag{A2}$$

We can now estimate all the factors on the right-hand side from the simulation result and reconstruct the explicit dependence of f on ν. Note that it follows immediately from Equation A2 that for quantities f that do not depend on c the second term vanishes and that thus the explicit and the total dependence of f on ν are the same. In order to illustrate the explicit effect of ν on f in the different figures, we are now going to build a corrected function $\widetilde{f}_\alpha$, where the subscript α denotes that the function depends on the value of the amplitude of the evaporation forcing as a parameter.

Since the dependence of c on ν is weak at high wavenumbers, we are going to assume that for $\nu = 10\widetilde{f}$ is equal to f, so

$$f(c(\nu=10,\alpha),\nu=10)=\widetilde{f}_\alpha(\nu=10). \tag{A3}$$

We then calculate recursively the values of $\widetilde{f}_\alpha$ by setting

$$\widetilde{f}_\alpha(\nu_j)=\widetilde{f}_\alpha(\nu_{j+1})-\int_{\nu_j}^{\nu_{j+1}}\frac{\partial f(c(\nu,\alpha),\nu)}{\partial \nu}d\nu. \tag{A4}$$

Applying Equation A2 to the right-hand side of the equation then yields

$$\widetilde{f}_\alpha(\nu_j)=\widetilde{f}_\alpha(\nu_{j+1})-\int_{\nu_j}^{\nu_{j+1}}\left(\frac{df(c(\nu,\alpha),\nu)}{d\nu}-\frac{\partial f(c(\nu,\alpha),\nu)}{\partial c}\cdot\frac{dc(\nu,\alpha)}{d\nu}\right)d\nu. \tag{A5}$$

Applying the fundamental theorem of calculus yields

$$\widetilde{f}_\alpha(\nu_j)=\widetilde{f}_\alpha(\nu_{j+1})-(f(c(\nu_{j+1},\alpha),\nu_{j+1})-f(c(\nu_j,\alpha),\nu_j))+\int_{\nu_j}^{\nu_{j+1}}\frac{\partial f(c(\nu,\alpha),\nu)}{\partial c}\cdot\frac{dc(\nu,\alpha)}{d\nu}d\nu. \tag{A6}$$

We assume now that the principal dependence of f on c is explicit, meaning that

$$\frac{df(c(\nu,\alpha),\nu)}{dc}\approx\frac{\partial f(c(\nu,\alpha),\nu)}{\partial c}. \tag{A7}$$

In cases where f has a strong dependence on c, the dependence tends to be linear (Figure 3 and Table 1). We therefore assume

$$\frac{\partial f(c(\nu,\alpha),\nu)}{\partial c}=r, \tag{A8}$$

where r is the regression coefficient of f onto c. Applying this to Equation A6 yields

$$\widetilde{f}_\alpha(\nu_j)=\widetilde{f}_\alpha(\nu_{j+1})-(f(c(\nu_{j+1},\alpha),\nu_{j+1})-f(c(\nu_j,\alpha),\nu_j))+r\int_{\nu_j}^{\nu_{j+1}}\frac{dc(\nu,\alpha)}{d\nu}d\nu. \tag{A9}$$

We apply again the fundamental theorem of calculus to Equation A9 and obtain

$$\widetilde{f}_\alpha(\nu_j)=\widetilde{f}_\alpha(\nu_{j+1})-(f(c(\nu_{j+1},\alpha),\nu_{j+1})-f(c(\nu_j,\alpha),\nu_j))+r(c(\nu_{j+1},\alpha)-c(\nu_j,\alpha)). \tag{A10}$$

Equations A10 and A3 allow us thus to calculate the corrected function $\widetilde{f}_\alpha$.

Appendix B: Removing the Implicit Impact of the Average Zonal Size of Subsidence Regions Through Its Effect on the Convective Fraction

In order to remove the impact of the average zonal size of subsidence regions L_D through the convective fraction c on a variable f that depends on L_D and on the convective fraction, we will proceed in a similar manner as we did in Appendix A. We first note that L_D is defined as

$$L_D = 360\frac{(1-c)}{\nu}. \tag{B1}$$

For the CONTROL and the CONSTANT experiment we assume $L_D = 0$. The change of f with L_D in our problem is

$$\frac{df(c(L_D),\, L_D)}{dL_D} = \frac{\partial f(c(L_D),\, L_D)}{\partial c}\cdot\frac{dc(L_D)}{dL_D} + \frac{\partial f(c(L_D),\, L_D)}{\partial L_D}. \tag{B2}$$

We note that the problem is similar in structure as in Appendix A, and we can thus use a similar approach to build a corrected function that we denote with$\hat{f}$. We choose ν10-α8 to be the reference experiment:

$$f(c(L_D(\nu = 10,\ \alpha = 8)),\ L_D(\nu = 10,\ \alpha = 8)) = \hat{f}(L_D(\nu = 10,\ \alpha = 8)). \tag{B3}$$

Since L_D is strictly different in every experiment, the function$\hat{f}$ is injective and thus does not depend on any parameter (unlike in the case of$\widetilde{f}_\alpha$ discussed in Appendix A).

We define now similarly as in Appendix A the values of $\hat{f}$ recursively:

$$\hat{f}(L_{Dj}) = \hat{f}(L_{Dj+1}) - \int_{L_{Dj}}^{L_{Dj+1}} \frac{\partial f(c(L_D),\, L_D)}{\partial L_D} dL_D. \tag{B4}$$

Performing the same transformations as in Appendix A for $\widetilde{f}_\alpha$ to Equation B4for $\hat{f}$, we obtain

$$\hat{f}(L_{Dj+1}) = \hat{f}(L_{Dj+1}) - (f(c(L_{Dj+1}),\, L_{Dj+1}) - f(c(L_{Dj}),\, L_{Dj})) + \int_{L_{Dj}}^{L_{Dj+1}} \frac{\partial f(c(L_D),\, L_D)}{\partial c}\cdot\frac{dc(L_D)}{dL_D} dL_D. \tag{B5}$$

We now need to find an expression for the partial derivative of f with respect to c. We start from

$$\frac{df(c(\text{Ł}_D),\, L_D)}{dc} = \frac{\partial f(c(L_D),\, L_D)}{\partial c} + \frac{\partial f(c(L_D),\, L_D)}{\partial L_D}\cdot\frac{dL_D}{dc}. \tag{B6}$$

Unlike in Appendix A we cannot just neglect the second term on the right-hand side of Equation B6, because L_D is proportional to c according to Equation B1. We note that

$$\frac{dL_D}{dc} \approx \frac{-360}{\nu}, \tag{B7}$$

and that

$$\frac{\partial}{\partial L_D} = \frac{\nu}{-360}\frac{\partial}{\partial c}, \tag{B8}$$

and so

$$\frac{\partial f(c(L_D),\, L_D)}{\partial L_D}\cdot\frac{dL_D}{dc} \approx \frac{\partial f(c(L_D),\, L_D)}{\partial c}. \tag{B9}$$

We can thus rewrite Equation B6 as

$$\frac{df(c(\text{Ł}_D), L_D)}{dc} = 2\frac{\partial f(c(L_D), L_D)}{\partial c} = r, \tag{B10}$$

where we assumed again (like in Appendix A) that f is a linear function of c and that r is the regression coefficient of f onto c. We can thus rewrite Equation B5 as

$$\hat{f}(L_{Dj+1}) = \hat{f}(L_{Dj+1}) - (f(c(L_{Dj+1}), L_{Dj+1}) - f(c(L_{Dj}), L_{Dj})) + \frac{r}{2}\int_{L_{Dj}}^{L_{Dj+1}} \frac{dc(L_D)}{dL_D} dL_D. \tag{B11}$$

Applying the fundamental theorem of calculus to Equation A9, we finally obtain

$$\hat{f}(L_{Dj+1}) = \hat{f}(L_{Dj+1}) - (f(c(L_{Dj+1}), L_{Dj+1}) - f(c(L_{Dj}), L_{Dj})) + \frac{r}{2}(c(L_{Dj+1}) - c(L_{Dj})). \tag{B12}$$

Equations B12 and B3 allow us thus to calculate the corrected function $\hat{f}$.

Data Availability Statement

The version of the LMDZ model used for this study including the scripts to create the evaporation patterns and other files necessary to repeat the simulations, scripts used to create figures and other analysis, and essential model output is publicly available on the Zendoo repository: https://zenodo.org/record/3924661 (DOI: 10.5281/zenodo.3924661).

Acknowledgments

We thank Caroline Muller, Kuniaki Inoue, and two reviewers for constructive discussions and valuable suggestions. This project has received funding from the European Research Council (ERC) under the European Union's Horizon 2020 research and innovation programme (Grant Agreement 694768). This work was granted access to the HPC resources of IDRIS under the allocation 0292 made by GENCI. M. P. acknowledges funding from the Centre national d' études spatiales (CNES).

References

Adam, O. (2018). Zonally varying ITCZS in a Matsuno-Gill-type model with an idealized Bjerknes feedback. *Journal of Advances in Modeling Earth Systems*, *10*, 1304–1318. https://doi.org/10.1029/2017MS001183

Adam, O., Bischoff, T., & Schneider, T. (2016). Seasonal and interannual variations of the energy flux equator and ITCZ. Part I: Zonally averaged ITCZ position. *Journal of Climate*, *29*(9), 3219–3230.

Adames, A. F., & Kim, D. (2016). The MJO as a dispersive, convectively coupled moisture wave: Theory and observations. *Journal of the Atmospheric Sciences*, *73*(3), 913–941.

Adames, A. F., & Ming, Y. (2018a). Interactions between water vapor and potential vorticity in synoptic-scale monsoonal disturbances: Moisture vortex instability. *Journal of the Atmospheric Sciences*, *75*(6), 2083–2106.

Adames, A. F., & Ming, Y. (2018b). Moisture and moist static energy budgets of South Asian monsoon low pressure systems in GFDL AM4.0. *Journal of the Atmospheric Sciences*, *75*(6), 2107–2123.

Arnold, N. P., & Randall, D. A. (2015). Global-scale convective aggregation: Implications for the Madden-Julian Oscillation. *Journal of Advances in Modeling Earth Systems*, *7*, 1499–1518. https://doi.org/10.1002/2015MS000498

Arnold, N. P., Tziperman, E., & Farrell, B. (2012). Abrupt transition to strong superrotation driven by equatorial wave resonance in an idealized GCM. *Journal of the Atmospheric Sciences*, *69*(2), 626–640.

Back, L. E., & Bretherton, C. S. (2006). Geographic variability in the export of moist static energy and vertical motion profiles in the tropical Pacific. *Geophysical Research Letters*, *33*, L17810. https://doi.org/10.1029/2006GL026672

Bellon, G., & Sobel, A. H. (2010). Multiple equilibria of the Hadley circulation in an intermediate-complexity axisymmetric model. *Journal of Climate*, *23*(7), 1760–1778.

Bretherton, C. S., Blossey, P. N., & Khairoutdinov, M. (2005). An energy-balance analysis of deep convective self-aggregation above uniform SST. *Journal of the Atmospheric Sciences*, *62*(12), 4273–4292.

Coppin, D., & Bony, S. (2015). Physical mechanisms controlling the initiation of convective self-aggregation in a general circulation model. *Journal of Advances in Modeling Earth Systems*, *7*, 2060–2078. https://doi.org/10.1002/2015MS000571

Coppin, D., & Bony, S. (2017). Internal variability in a coupled general circulation model in radiative-convective equilibrium. *Geophysical Research Letters*, *44*, 5142–5149. https://doi.org/10.1002/2017GL073658

Dufresne, J.-L. (2013). Climate change projections using the IPSL-CM5 Earth System Model: From CMIP3 to CMIP5. *Climate Dynamics*, *40*(9-10), 2123–2165.

Emanuel, K. A. (1987). An air-sea interaction model of intraseasonal oscillations in the tropics. *Journal of the Atmospheric Sciences*, *44*(16), 2324–2340.

Emanuel, K. A., Neelin, D. J., & Bretherton, C. S. (1994). On large-scale circulations in convecting atmospheres. *Quarterly Journal of the Royal Meteorological Society*, *120*(519), 1111–1143.

Emanuel, K. A., & Živković-Rothman, M. (1999). Development and evaluation of a convection scheme for use in climate models. *Journal of the Atmospheric Sciences*, *56*(11), 1766–1782.

Fläschner, D., Mauritsen, T., Stevens, B., & Bony, S. (2018). The signature of shallow circulations, not cloud radiative effects, in the spatial distribution of tropical precipitation. *Journal of Climate*, *31*(23), 9489–9505.

Gastineau, G., Li, L., & Treut, H. L. (2011). Some atmospheric processes governing the large-scale tropical circulation in idealized aquaplanet simulations. *Journal of the Atmospheric Sciences*, *68*(3), 553–575.

Gill, A. E. (1980). Some simple solutions for heat-induced tropical circulation. *Quarterly Journal of the Royal Meteorological Society*, *106*(449), 447–462.

Gruber, A. (1972). Fluctuations in the position of the ITCZ in the Atlantic and Pacific Oceans. *Journal of the Atmospheric Sciences*, *29*, 193–196.

Harrop, B. E., & Hartmann, D. L. (2016). The role of cloud radiative heating in determining the location of the ITCZ in aquaplanet simulations. *Journal of Climate*, *29*(8), 2741–2763.

Held, I. M., Hemler, R. S., & Ramaswamy, V. (1993). Radiative-convective equilibrium with explicit two-dimensional moist convection. *Journal of the Atmospheric Sciences*, *50*(23), 3909–3927.

Holloway, C. E., Wing, A. A., Bony, S., Muller, C., Masunaga, H., L'Ecuyer, T. S., et al. (2017). Observing convective aggregation. *Surveys in Geophysics*, *38*(6), 1199–1236.

Hourdin, F. (2013). Impact of the LMDZ atmospheric grid configuration on the climate and sensitivity of the IPSL-CM5A coupled model. *Climate Dynamics*, *40*(9-10), 2167–2192.

Hourdin, F., Musat, I., Bony, S., Braconnot, P., Codron, F., Dufresne, J.-L., et al. (2006). The LMDZ4 general circulation model: Climate performance and sensitivity to parametrized physics with emphasis on tropical convection. *Climate Dynamics*, *27*(7-8), 787–813.

Houze, R. A. (1977). Structure and dynamics of a tropical squall line system. *Monthly Weather Review*, *105*(12), 1540–1567.

Hwang, Y.-T., & Frierson, D. M. W. (2013). Link between the double-Intertropical Convergence Zone problem and cloud biases over the Southern Ocean. *Proceedings of the National Academy of Sciences*, *110*(13), 4935–4940.

Inoue, K., & Back, L. E. (2015). Gross moist stability assessment during TOGA COARE: Various interpretations of gross moist stability. *Journal of the Atmospheric Sciences*, *72*(11), 4148–4166.

Kang, S. M., Held, I. M., Frierson, D. M. W., & Zhao, M. (2008). The response of the ITCZ to extratropical thermal forcing: Idealized slab-ocean experiments with a GCM. *Journal of Climate*, *21*(14), 3521–3532.

Laing, A. G., & Fritsch, J. M. (1997). The global population of mesoscale convective complexes. *Quarterly Journal of the Royal Meteorological Society*, *123*(538), 389–405.

Lindzen, R. S., & Hou, A. V. (1988). Hadley circulations for zonally averaged heating centered off the equator. *Journal of the Atmospheric Sciences*, *45*(17), 2416–2427.

Lutsko, N. J. (2018). The response of an idealized atmosphere to localized tropical heating: Superrotation and the breakdown of linear theory. *Journal of the Atmospheric Sciences*, *75*(1), 3–20.

Möbis, B., & Stevens, B. (2012). Factors controlling the position of the Intertropical Convergence Zone on an aquaplanet. *Journal of Advances in Modeling Earth Systems*, *4*, M00A04. https://doi.org/10.1029/2012MS000199

Madden, R. A., & Julian, P. R. (1971). Detection of a 4050 day oscillation in the zonal wind in the tropical Pacific. *Journal of the Atmospheric Sciences*, *28*(5), 702–708.

Madden, R. A., & Julian, P. R. (1994). Observations of the 4050-day tropical oscillation—A review. *Monthly Weather Review*, *122*(5), 814–837.

Mapes, B. E., & Houze, R. A. (1993). Cloud clusters and superclusters over the oceanic warm pool. *Monthly Weather Review*, *121*(5), 1398–1416.

Matsuno, T. (1966). Quasi-geostrophic motions in the equatorial area. *Journal of the Meteorological Society of Japan*, *44*(1), 25–43.

Muller, C., & Bony, S. (2015). What favors convective aggregation and why? *Geophysical Research Letters*, *42*, 5626–5634. https://doi.org/10.1002/2015GL064260

Muller, C. J., & Held, I. M. (2012). Detailed investigation of the self-aggregation of convection in cloud-resolving simulations. *Journal of the Atmospheric Sciences*, *69*(8), 2551–2565.

Neale, R. B., & Hoskins, B. J. (2000). A standard test for AGCMs including their physical parametrizations: I: The proposal. *Atmospheric Science Letters*, *1*(2), 101–107.

Neelin, J. D., Held, I. M., & Cook, K. H. (1987). Evaporation-wind feedback and low-frequency variability in the tropical atmosphere. *Journal of the Atmospheric Sciences*, *44*(16), 2341–2348.

Oueslati, B., & Bellon, G. (2013). Tropical precipitation regimes and mechanisms of regime transitions: Contrasting two aquaplanet general circulation models. *Climate Dynamics*, *40*(9-10), 2345–2358.

Pendergrass, A. G. (2020). Changing degree of convective organization as a mechanism for dynamic changes in extreme precipitation. Current Climate Change Reports.

Pendergrass, A. G., Reed, K. A., & Medeiros, B. (2016). The link between extreme precipitation and convective organization in a warming climate: Global radiative-convective equilibrium simulations. *Geophysical Research Letters*, *43*, 11,445–11,452. https://doi.org/10.1002/2016GL071285

Pierrehumbert, R. T. (1998). Lateral mixing as a source of subtropical water vapor. *Geophysical Research Letters*, *25*(2), 151–154.

Popp, M., & Bony, S. (2019). The impact of convective clustering on the width of the tropical rain belt. *Nature Communications*, *10*(4261).

Popp, M., & Lutsko, N. J. (2017). Quantifying the zonal-mean structure of tropical precipitation. *Geophysical Research Letters*, *44*, 9470–9478. https://doi.org/10.1002/2017GL075235

Popp, M., & Silvers, L. G. (2017). Double and single ITCZs with and without clouds. *Journal of Climate*, *30*(22), 9147–9166.

Privé, N. C., & Plumb, R. A. (2007). Monsoon dynamics with interactive forcing. Part I: Axisymmetric studies. *Journal of the Atmospheric Sciences*, *64*(5), 1417–1430.

Romps, D. M. (2014). An analytical model for tropical relative humidity. *Journal of Climate*, *27*(19), 7432–7449.

Schneider, T., Bischoff, T., & Haug, G. H. (2014). Migrations and dynamics of the intertropical convergence zone. *Nature*, *513*(7516), 45–53.

Semie, A. G., & Bony, S. (2020). Relationship between precipitation extremes and convective organization inferred from satellite observations. *Geophysical Research Letters*, *47*, e2019GL086927. https://doi.org/10.1029/2019GL086927

Sherwood, S. C., Ingram, W., Tsushima, Y., Satoh, M., Roberts, M., Vidale, P. L., & O'Gorman, P. A. (2010). Relative humidity changes in a warmer climate. *Journal of Geophysical Research*, *115*, D09104. https://doi.org/10.1029/2009JD012585

Showman, A. P., & Polvani, L. M. (2010). The Matsuno-Gill model and equatorial superrotation. *Geophysical Research Letters*, *37*, L18811. https://doi.org/10.1029/2010GL044343

Slingo, A., & Slingo, J. M. (1988). The response of a general-circulation model to cloud longwave radiative forcing. 1: Introduction and initial experiments. *Quarterly Journal of the Royal Meteorological Society*, *114*(482), 1027–1062.

Sobel, A. H., & Bretherton, C. S. (2000). Modeling tropical precipitation in a single column. *Journal of Climate*, *13*(24), 4378–4392.

Sobel, A. H., & Maloney, E. (2012). An idealized semi-empirical framework for modeling the Madden Julian Oscillation. *Journal of the Atmospheric Sciences*, *69*(5), 1691–1705.

Taylor, K. E., Stouffer, R. J., & Meehl, G. A. (2012). An overview of CMIP5 and the experiment design. *Bulletin of the American Meteorological Society*, *93*(4), 485–498.

Tobin, I., Bony, S., Holloway, C. E., Grandpeix, J.-Y., Sèze, G., Coppin, D., et al. (2013). Does convective aggregation need to be represented in cumulus parameterizations? *Journal of Advances in Modeling Earth Systems*, *5*, 692–703. https://doi.org/10.1002/jame.20047

Tobin, I., Bony, S., & Roca, R. (2012). Observational evidence for relationships between the degree of aggregation of deep convection, water vapor, surface fluxes, and radiation. *Journal of Climate*, *25*(20), 6885–6904.

Tompkins, A. M., & Craig, G. C. (1998). Radiative convective equilibrium in a three-dimensional cloud-ensemble model. *Quarterly Journal of the Royal Meteorological Society*, *124*(550), 2073–2097.

Tompkins, A. M., & Semie, A. G. (2016). Organization of tropical convection in low vertical wind shears: Role of updraft entrainment. *Journal of Advances in Modeling Earth Systems*, *9*, 1046–1068. https://doi.org/10.1002/2016MS000802

Waliser, D. E., & Gautier, C. (1993). A satellite-derived climatology of the ITCZ. *Journal of Climate*, *6*(11), 2162–2174.

Wei, H.-H., & Bordoni, S. (2018). Energetic constraints on the ITCZ position in idealized simulations with a seasonal cycle. *Journal of Advances in Modeling Earth Systems*, *10*, 1708–1725. https://doi.org/10.1029/2018MS001313

Williamson, D. (2012). The APE atlas (*NCAR/TN-484+STR*): National Center for Atmospheric Research.

Wing, A. A., & Cronin, T. W. (2016). Self-aggregation of convection in long channel geometry. *Quarterly Journal of the Royal Meteorological Society*, *142*(694), 1–15.

Wing, A. A., & Emanuel, K. A. (2014). Physical mechanisms controlling self-aggregation of convection in idealized numerical modeling simulations. *Surveys in Geophysics*, *6*, 59–74. https://doi.org/10.1007/s10712-017-9408-4

Wing, A. A., Emanuel, K., Holloway, C. E., & Muller, C. (2017). Convective self-aggregation in numerical simulations: A review. *Surveys in Geophysics*, *38*(6), 1173–1197.